REGULAR ARTICLE

WILEY

A 3D reactive collision avoidance algorithm for underactuated underwater vehicles

Martin S. Wiig[1] | Kristin Y. Pettersen[1] | Thomas R. Krogstad[2]

[1]Centre for Autonomous Marine Operations
and Systems (NTNU AMOS), Department of
Engineering Cybernetics, Norwegian
University of Science and Technology,
Trondheim, Norway

[2]Department of Defence System, Norwegian
Defence Research Establishment (FFI), Kjeller,
Norway

Correspondence
Martin S. Wiig, Centre for Autonomous Marine
Operations and Systems (NTNU AMOS),
Department of Engineering Cybernetics,
Norwegian University of Science and
Technology, 7491 Trondheim, Norway.
Email: Martin-Syre.Wiig@ffi.no

Funding information
Research Council of Norway,
Grant/Award Number: 223254—NTNU AMOS

Abstract

Avoiding collisions is an essential goal of the control system of autonomous vehicles. This paper presents a reactive algorithm for avoiding obstacles in a three-dimensional space, and shows how the algorithm can be applied to an underactuated underwater vehicle. The algorithm is based on maintaining a constant avoidance angle to the obstacle, which ensures that a guaranteed minimum separation distance is achieved. The algorithm can thus be implemented without knowledge of the obstacle shape. The avoidance angle is designed to compensate for obstacle movement, and the flexibility of operating in 3D can be utilized to implement traffic rules or operational constraints. We exemplify this by incorporating safety constraints on the vehicle pitch and by making the vehicle seek to move behind the obstacle, while also minimizing the required control effort. The underactuation of the vehicle induces a sway and heave movement while turning. To avoid uncontrolled gliding into the obstacle, we account for this movement using a Flow frame controller, which controls the direction of the vehicle's velocity rather than just the pitch and yaw. We derive conditions under which it is ensured that the resulting maneuver is safe, and these results are verified trough simulations and through full-scale experiments on the Hugin HUS autonomous underwater vehicle. The latter demonstrates the performance of the proposed algorithm when applied to a case with unmodeled disturbances and sensor noise, and shows how the modular nature of the collision avoidance algorithm allows it to be applied on top of a commercial control system.

1 | INTRODUCTION

Unmanned vehicles are often intended to operate with limited, delayed, or no human supervision. The environment they operate in can be dynamic or unknown, with only incomplete or partially erroneous a priori information available. This is often the scenario for autonomous underwater vehicles (AUVs), charged with exploration and mapping of the world's oceans. The autonomous nature of AUV missions necessitates the ability to react to the environment, for example, to avoid collision

with obstacles. The collision avoidance problem becomes particularly challenging if the vehicle is underactuated, as indeed many AUVs are. An underactuated vehicle is not able to control all degrees of freedom independently, and generally has second-order nonholonomic constraints, making it necessary to include the vehicle dynamics in the design and analysis of the control system (Pettersen & Egeland, 1996). In this paper, we present and analyze a collision avoidance algorithm called the constant avoidance angle algorithm, which we have implemented on a class of underactuated underwater vehicles.

The collision avoidance problem has been fairly well studied, particularly in 2D, with surveys of existing algorithms given in Hoy, Matveev, and Savkin (2014), Statheros, Howells, and Maier (2008), and Tam, Bucknall, and Greig (2009). The various algorithms are often sorted into two families; reactive algorithms and motion planning algorithms. Motion planning algorithms include model predictive control (Chen, Peng, & Grizzle, 2018; Hagen, Kufoalor, Brekke, & Johansen, 2018; Johansen, Perez, & Cristofaro, 2016) and the faster dynamic window algorithm (Eriksen, Breivik, Pettersen, & Wiig, 2016, 2018; Fox, Burgard, & Thrun, 1997). Such algorithms can, particularly in 3D, become computationally intractable for vehicles with limited processing power, as the general motion planning problem has been shown to be NP-hard (Canny & Reif, 1987). Furthermore, for vehicles capable of implementing motion planning, a safety critical function such as collision avoidance requires a level of redundancy, which can be achieved by having a computationally simpler, yet provably safe, algorithm as a backup. Thus, there is a need for reactive algorithms.

A canonical reactive approach to collision avoidance is the artificial potential field method (Khatib, 1986), and its extension of navigation functions (Roussos, Dimarogonas, & Kyriakopoulos, 2010) and navigation vector fields (Panagou, 2014). While these algorithms are intuitive and easy to extend to custom scenarios, they often rely on an underlying assumption that the vehicle is always able to follow the gradient of the field. Furthermore, the effect of the underlying vehicle dynamics, particularly in the case of underactuated vehicles, tends to be neglected in the analysis.

Two equivalent methods inherently considering moving obstacles are velocity obstacles (Fiorini & Shiller, 1998) and collision cones (Chakravarthy & Ghose, 1998). These methods divide a 2D velocity space into safe and unsafe velocities, and collision avoidance is usually achieved by choosing the closest safe velocity. The velocity obstacle approach has been extended to include acceleration constraints (van den Berg, Snape, Guy, & Manocha, 2011) and general vehicle dynamics (Wilkie, Van Den Berg, & Manocha, 2009). However, the latter is not trivial for vehicles with complex dynamics, while the former becomes restrictive for vehicles with a limited speed envelope. Both of these constraints are present in underactuated AUVs.

The velocity obstacle approach is elegantly extended to 3D in Jenie, Van Kampen, de Visser, Ellerbroek, and Hoekstra (2015) and Jenie, van Kampen, de Visser, Ellerbroek, and Hoekstra (2016). Here, the 3D velocity space is divided into a set of discrete planes, and the 2D velocity obstacle approach is applied to each plane. This is an intuitive extension, but the problems pertaining to vehicle constraints and dynamics in the velocity obstacle approach remain unaddressed.

The collision cone approach is extended to 3D in Lalish and Morgansen (2012), where a multiagent system can be made to provably reach and remain in a conflict-free state. Both limited speed envelopes and acceleration constraints are included, making the results very solid. Vehicle dynamics is, however, not explicitly accounted for, which may be a problem for underactuated vehicles.

The authors of Savkin and Wang (2013) propose an algorithm which makes a unicycle-type vehicle provably avoid a moving obstacle. The algorithm makes the vehicle keep a constant avoidance angle to the obstacle, and compensates this angle for the obstacle velocity. This approach has the advantage that knowledge of the obstacle shape is not required for implementation, only the vision cone to the obstacle. However, while the algorithm provides safe heading references, it also imposes a strict requirement on the vehicle speed trajectory during the avoidance maneuver. The flexibility to design the speed trajectory of the vehicle independently is thus removed, which complicates the implementation on underactuated vehicles and is a significant drawback for vehicles with a limited speed envelope. Furthermore, the vehicle dynamics is not considered, and the speed requirement also leads to a singularity in the required yaw rate.

The constant avoidance angle algorithm is extended to 3D in Wang, Savkin, and Garrett (2018). Here, a plane is created containing the vehicle, the obstacle and the vehicle's velocity vector. The vehicle will operate in this plane, employing the algorithm from Savkin and Wang (2013) to avoid the obstacle. While this is an intuitive extension, it does not fully exploit the 3D structure of the system, and the issues of the 2D algorithm have not been addressed.

A new constant avoidance angle algorithm is proposed in Wiig, Pettersen, and Krogstad (2019). This algorithm provides a safe heading for a given desired forward (surge) speed trajectory. This is exemplified by restricting the vehicle to keep a constant desired surge speed, demonstrating that the algorithm is suitable for vehicles with a limited speed envelope. The complete 3 degree of freedom (DOF) dynamics of an underactuated marine vehicle is included in the design and analysis of the algorithm and the underlying control system. In particular, the underactuated sideways (sway) dynamics is accounted for by steering the direction of the vehicle's velocity vector rather than the vehicle heading directly. The sway dynamics gives rise to an underactuated component in the vehicle speed, which the new formulation of the algorithm easily accounts for. Both vehicle safety and the well definedness of the control signals are proven.

In this paper, we extend the constant avoidance angle algorithm in Wiig et al. (2019) to 3D. In short, the algorithm we propose creates a cone of velocity directions which are safe at the current speed, and the full flexibility offered by operating in 3D space is utilized when choosing among them. The work builds on the preliminary contributions presented in Wiig, Pettersen, and Krogstad (2018a, 2018b). The 3D cone of safe directions keeping a constant avoidance angle to the obstacle is introduced in Wiig et al. (2018a). Pitch limitations, which are often present for safety reasons in vehicles such as AUVs, are included in the algorithm, which operates on a kinematic vehicle modeled with nonholonomic constraints and limitations on the turning and pitching rates.

Only the vehicle kinematics was considered in Wiig et al. (2018a). In Wiig et al. (2018b), the design and analysis of the algorithm also included the important underactuated dynamics of an underactuated marine vehicle. This necessitates the design of a Flow frame controller, a controller steering the direction of the vehicle's velocity vector. This is a 3D extension of the course controller

presented in Wiig et al. (2019), an extension which is nontrivial due to the presence of composite rotations in 3D. Conditions are given under which the Flow frame controller is feasible, and under which obstacle avoidance is still guaranteed, despite the underactuation.

The preliminary results are incorporated into this paper, where we further extend the control system to consider the full 5 DOF dynamics of a vehicle operating at maneuvering speed. By smoothing the required pitch and yaw rate during the discrete switch from nominal operation when starting the collision avoidance maneuver, we ensure that all the control signals in the system remain well defined. Furthermore, while Wiig et al. (2018a, 2018b) only considered static obstacles, we will in this paper extend the algorithm to also include moving obstacles by compensating the cone of safe directions for the obstacle's velocity. The compensation is dependent also on the vehicle speed, which contains an underactuated component when the vehicle is turning. We show how this component is inherently accounted for by the algorithm, and provide conditions under which the avoidance maneuver is still provably safe. This obstacle velocity compensation is an extension of the technique used in 2D in Wiig et al. (2019); if both the vehicle and the obstacle moves in the same horizontal plane without pitching they are equivalent. By extending the technique to 3D, we are able to consider the obstacle velocity also when utilizing the added maneuvering flexibility.

We are, in this study, mainly concerned with the avoidance of sparsely spaced obstacles, and thus an analysis of multiobstacle scenarios is beyond the current scope. However, it is possible to extend the algorithm to include multiple moving hindrances. We will provide a qualitative description of this process, and will demonstrate its applicability in numerical simulations.

The algorithm has been implemented into the control system of a Hugin AUV (Hagen, Storkersen, Vestgard, & Kartvedt, 2003), which is a commercially widespread AUV jointly developed by the Norwegian Defense Research Establishment and Kongsberg Maritime. Even though access to the low level control system was not available, the modular nature of the algorithm made it straight forward to implement it on top of the existing control system. To demonstrate the algorithm capabilities in a controlled manner, the vehicle was made to avoid moving obstacles in a sequence of several experiments with time-varying parameters. The vehicle was able to avoid all the obstacles, even in the presence of sensor noise and unmodeled environmental disturbances. This implies robustness of the algorithm from a control perspective, an implication which is strengthened by a set of Monte Carlo simulations adding probabilistic perturbation to the dynamic model used by the underlying controllers.

The remainder of this paper is organized as follows. In Section 2 we provide some brief mathematical preliminaries and notations, before we present the vehicle model in Section 3. Section 4 states the controllers for the direction of the velocity vector, the guidance law employed to steer the vehicle toward a target and the low level controllers. The collision avoidance algorithm itself is described in Section 5, before an analysis of the system is given in Section 6. The analysis is validated by simulations in Section 7 and through experiments in Section 8. Finally, concluding remarks and thoughts on future work are given in Section 9.

2 | MATHEMATICAL PRELIMINARIES

The trigonometric functions $\sin(\cdot)$, $\cos(\cdot)$, and $\tan(\cdot)$ will be denoted $s(\cdot)$, $c(\cdot)$, and $t(\cdot)$, respectively.

A general vector $\boldsymbol{u}$ in a reference frame a is denoted $\boldsymbol{u}^a$. The position of a reference frame o with respect to n is denoted $\boldsymbol{p}_o^n$. A velocity vector of frame o with respect to n, represented in n is denoted $\boldsymbol{v}_{o/n}^n$, where the superscript ^{n} signifies that the velocity is represented in n, while the subscript $_{o/n}$ signifies that the vector holds the velocity of o with respect to n.

The rotation matrix from reference frame a to a frame b is denoted $\boldsymbol{R}_a^b$, so that $\boldsymbol{u}^b = \boldsymbol{R}_a^b \boldsymbol{u}^a$, while the rotation matrix $\boldsymbol{R}_{zyx}(\varphi, \theta, \psi)$ represents a composite rotation using the zyx-convention and the Euler angles φ(roll), θ (pitch), and ψ (yaw). For convenience, we also define $\boldsymbol{R}_{zy}(\theta, \psi) \triangleq \boldsymbol{R}_{zyx}(0, \theta, \psi)$ and $\boldsymbol{R}_z(\psi) \triangleq \boldsymbol{R}_{zyx}(0, 0, \psi)$. We denote the pitch of a frame b with respect to n as θ_b^n, and likewise for roll and yaw.

We denote the components of a vector $\boldsymbol{u}$ as u_x, u_y, and u_z, so that $\boldsymbol{u} = [u_x, u_y, u_z]^T$. Furthermore, we define the following functions converting $\boldsymbol{u}$ into a heading and a pitch angle:

$$\Psi(\boldsymbol{u}) = \text{atan2}(u_y, u_x), \tag{1}$$

$$\Theta(\boldsymbol{u}) = -\sin^{-1}\left(\frac{u_z}{\|\boldsymbol{u}\|}\right). \tag{2}$$

To get a measure of how much control effort is required to turn the vehicle into a desired direction, we define the angular distance between two vectors $\boldsymbol{u}_1$ and $\boldsymbol{u}_2$ as

$$\xi(\boldsymbol{u}_1, \boldsymbol{u}_2) \triangleq \sqrt{(\Psi(\boldsymbol{u}_2) - \Psi(\boldsymbol{u}_1))^2 + (\Theta(\boldsymbol{u}_2) - \Theta(\boldsymbol{u}_1))^2}. \tag{3}$$

2.1 | Reference frames

Throughout this paper we will use various reference frames to model the vehicle and the obstacle, and to describe the collision avoidance algorithm. In Table 1, we list the most important reference frames, along with a short summary of each.

3 | SYSTEM DESCRIPTION

3.1 | Basic assumptions

We will, in Section 3.2, model the vehicle using a maneuvering model (Fossen, 2011). The structure of the system matrices used in the model is dependent on a set of basic assumptions, which are listed here for convenience. These assumptions are valid for many commercial AUVs.

Assumption 1. The vehicle is symmetric in the x–z plane and in the x–y plane. Furthermore, the length-to-width ratio of the vehicle is large.

TABLE 1 Reference frames

Frame	Description
n	The inertial North-East-Down (NED) reference frame.
b	The Body reference frame, which is attached to and aligned with the vehicle.
f	The Flow reference frame, which is attached to the vehicle and aligned with the vehicle's velocity vector.
n_b	A Body-fixed reference frame oriented along the NED frame. This frame is used to represent positions relative to the vehicle.
o	The Obstacle reference frame, which is attached to the obstacle.
b_{vo}	A Body-fixed reference frame oriented such that its x-axis points toward the obstacle.

Assumption 2. The vehicle model is expressed the Body frame b, which is located on the center line of the vehicle. The distance from the center of gravity (CG) to the origin of b is $(x_g, 0, 0)$, and hence CG is also on the center line.

Assumption 3. The center of buoyancy (CB) and CG lies on the same vertical axis in b.

Assumption 4. Any nonlinear damping parameters can be neglected, so that only linear damping needs to be considered.

Assumption 5. The vehicle is passively stable in roll and roll motion can hence be neglected.

Assumption 6. The vehicle is neutrally buoyant.

Assumption 7. The control input in surge does not affect the other DOF. Furthermore, only couplings in sway-yaw and heave-pitch need to be considered.

Remark 1. Assumption 7 can be made for slender underwater vehicles, that is vehicles satisfying Assumption 1. These assumptions enable us to remove couplings between yaw and pitch movements in the model, thus simplifying the controller design and analysis.

3.2 | Vehicle model

By Assumption 5, the roll DOF can be removed, and we hence model the vehicle in 5 DOF. The position and orientation of the vehicle's Body frame b with respect to the inertial frame n is represented by the vector $\boldsymbol{\eta}_b^n \triangleq [\boldsymbol{p}_b^n, \theta_b^n, \psi_b^n]^T$, where $\boldsymbol{p}_b^n \triangleq [x_b^n, y_b^n, z_b^n]^T$. To transform

between b and n we use a transformation matrix $\boldsymbol{J}(\boldsymbol{\eta}_b^n)$, which is defined as

$$\boldsymbol{J}\left(\boldsymbol{\eta}_b^n\right) \triangleq \begin{bmatrix} \boldsymbol{R}_{zy}\left(\theta_b^n, \psi_b^n\right) & 0 \\ 0 & \boldsymbol{T}\left(\theta_b^n\right) \end{bmatrix}, \tag{4}$$

where $\boldsymbol{T}(\theta_b^n) \triangleq \mathrm{diag}(1, 1/\cos(\theta_b^n)), |\theta_b^n| \neq \frac{\pi}{2}$. The transformation matrix is used to obtain $\dot{\boldsymbol{\eta}}_b^n$ from the body-fixed velocity vector $\boldsymbol{\nu}_{b/n}^b \triangleq [\boldsymbol{v}_{b/n}^b, q_b, r_b]^T$, where $\boldsymbol{v}_{b/n}^b \triangleq [u_b, v_b, w_b]^T$ contains the speeds in surge u_b, sway v_b and heave w_b, while q_b is pitch rate and r_b is yaw rate. Thus, the vehicle kinematics are

$$\dot{\boldsymbol{\eta}}_b^n = \boldsymbol{J}\left(\boldsymbol{\eta}_b^n\right)\boldsymbol{\nu}_{b/n}^b. \tag{5}$$

The dynamics of the vehicle are obtained using a maneuvering model (Fossen, 2011):

$$\boldsymbol{M}\dot{\boldsymbol{\nu}}_{b/n}^b + \boldsymbol{C}\left(\boldsymbol{\nu}_{b/n}^b\right)\boldsymbol{\nu}_{b/n}^b + \boldsymbol{D}\boldsymbol{\nu}_{b/n}^b + \boldsymbol{g}\left(\boldsymbol{\eta}_b^n\right) = \boldsymbol{B}f, \tag{6}$$

where $\boldsymbol{M} = \boldsymbol{M}^T > 0$ is the mass and inertia matrix including hydrodynamic added mass, and $\boldsymbol{D}$ is the hydrodynamic damping matrix. The structure of $\boldsymbol{M}$ and $\boldsymbol{D}$ are obtained using Assumptions 1–4:

$$\boldsymbol{M} \triangleq \begin{bmatrix} m_{11} & 0 & 0 & 0 & 0 \\ 0 & m_{22} & 0 & 0 & m_{25} \\ 0 & 0 & m_{33} & m_{34} & 0 \\ 0 & 0 & m_{34} & m_{44} & 0 \\ 0 & m_{25} & 0 & 0 & m_{55} \end{bmatrix}, \quad \boldsymbol{D} \triangleq \begin{bmatrix} d_{11} & 0 & 0 & 0 & 0 \\ 0 & d_{22} & 0 & 0 & d_{25} \\ 0 & 0 & d_{33} & d_{34} & 0 \\ 0 & 0 & d_{43} & d_{44} & 0 \\ 0 & d_{25} & 0 & 0 & d_{55} \end{bmatrix}. \tag{7}$$

The Coriolis and centripetal matrix $\boldsymbol{C}$ is obtained from $\boldsymbol{M}$ as described in Fossen (2011):

$$\boldsymbol{C} \triangleq \begin{bmatrix} 0 & 0 & 0 & m_{33}w_b + m_{34}q_b & -m_{22}v_b - m_{25}r_b \\ 0 & 0 & 0 & 0 & m_{11}u_b \\ 0 & 0 & 0 & -m_{11}u_b & 0 \\ -m_{33}w_b - m_{34}q_b & 0 & m_{11}u_b & 0 & 0 \\ m_{22}v_b + m_{25}r_b & -m_{11}u_b & 0 & 0 & 0 \end{bmatrix}. \tag{8}$$

Since we assume that the vehicle is neutrally buoyant in Assumption 6, and since CG and CB are on the same z-axis in b by Assumption 3, the gravity restoration vector $\mathbf{g}$ can be constructed as $\mathbf{g}\left(\boldsymbol{\eta}_b^n\right) \triangleq [0, 0, 0, BG_z W \sin(\theta_b^n), 0]^T$, where BG_z is the vertical distance between the CG and the CB.

The control input vector $\mathbf{f} \triangleq [T_u, T_q, T_r]^T$ contains input in surge (T_u), pitch (T_q), and yaw (T_r). In a typical AUV, this will consist of propeller speed, and rudder and sternplane angles, which are converted to control forces and moments using the actuator configuration matrix $\mathbf{B}$. The structure of $\mathbf{B}$ follows from Assumption 7:

$$\mathbf{B} \triangleq \begin{bmatrix} b_{11} & 0 & 0 \\ 0 & 0 & b_{23} \\ 0 & b_{32} & 0 \\ 0 & b_{42} & 0 \\ 0 & 0 & b_{53} \end{bmatrix}. \tag{9}$$

By choosing the point x_g from Assumption 2 to lie on the pivot point of the ship, we ensure that $\mathbf{M}^{-1}\mathbf{B}\mathbf{f} = [\tau_u, 0, 0, \tau_q, \tau_r]^T$, where τ_u, τ_q, and τ_r are control signals in surge, pitch and yaw, respectively. This decoupling of the control input from the underactuated variables will simplify the design and analysis of the control system. The low-level controllers described in Section 4.4 will create these signals to control u_b, q_b, and r_b, that is the directly actuated dynamics of the vehicle. However, the sway v_b and heave w_b dynamics can not be directly controlled. This is clearly seen if we solve (6) for $\dot{\mathbf{v}}_{b/n}^b$, obtaining the dynamics in component form:

$$\dot{u}_b = F_{u_b}(u_b, v_b, w_b, r_b, q_b) + \tau_u, \tag{10a}$$

$$\dot{v}_b = X_v(u_b)r_b + Y_v(u_b)v_b, \tag{10b}$$

$$\dot{w}_b = X_w(u_b)q_b + Y_w(u_b)w_b + Z_w \sin\left(\theta_b^n\right), \tag{10c}$$

$$\dot{q}_b = F_{q_b}\left(\theta_b^n, u_b, w_b, q_b\right) + \tau_q. \tag{10d}$$

$$\dot{r}_b = F_{r_b}(u_b, v_b, r_b) + \tau_r. \tag{10e}$$

The functions F_{u_b}, X_v, Y_v, X_w, Y_w, Z_w, F_{q_b}, and F_{r_b} contain hydrodynamic parameters from $\mathbf{M}$ and $\mathbf{D}$, and are defined in Appendix A.

Even though sway and heave cannot be directly controlled, we can still ensure that these dynamics are nominally stable by making the following assumption, where $u_{\min} > 0$ is the minimum operational surge speed of the vehicle, below which the maneuvering model is no longer valid:

Assumption 8. The functions $Y_v(u_b)$ and $Y_w(u_b)$ are negative for all $u_b \geq u_{\min}$.

This assumption holds for most AUVs by design.

3.3 | The flow frame

The direction of the vehicle's velocity vector is of main interest to us when steering the vehicle to avoid an obstacle. Thus, we would like to represent the vehicle kinematics in such a way that we obtain

$$\dot{\mathbf{p}}_b^n = \mathbf{R}_f^n\left(\theta_f^n, \psi_f^n\right)\mathbf{v}_{f/n}^f, \tag{11}$$

where $\mathbf{v}_{f/n}^f \triangleq [U_b, 0, 0]^T$ and $U_b \triangleq \|\mathbf{v}_{b/n}^b\|$. The frame f is called the Flow frame (Fossen, 2011), and the rotation from b to f is found using the angle of attack $\alpha_b \triangleq \operatorname{atan2}(w_b, u_b)$ and sideslip angle $\beta_b \triangleq \operatorname{atan2}(v_b, U_w)$, where $U_w \triangleq \sqrt{u_b^2 + w_b^2}$:

$$\mathbf{R}_b^f \triangleq \mathbf{R}_{zy}(\alpha_b, -\beta_b). \tag{12}$$

The vehicle kinematics can then be written as

$$\dot{\mathbf{p}}_b^n = \mathbf{R}_{zy}\left(\theta_b^n, \psi_b^n\right)\mathbf{R}_{zy}(\alpha_b, -\beta_b)^T\mathbf{v}_{f/n}^f. \tag{13}$$

The variables of the Flow frame are illustrated in Figure 1. To steer the Flow frame, we require expressions for the Euler angles φ_f^n, θ_f^n, and ψ_f^n, as well as the Flow frame angular velocity vector $\boldsymbol{\omega}_{f/n}^f \triangleq [p_f, q_f, r_f]^T$ containing the roll, pitch, and yaw rate, respectively. Using the procedure from Fossen (2011), the Euler angles are found as

$$\varphi_f^n = \tan^{-1}[s(\beta_b)t(\gamma_b)], \tag{14}$$

$$\theta_f^n = \sin^{-1}[c(\beta_b)s(\gamma_b)], \tag{15}$$

$$\psi_f^n = \tan^{-1}\left(\frac{c(\gamma_b)s\left(\psi_b^n\right)c(\beta_b) + c\left(\psi_b^n\right)s(\beta_b)}{c(\gamma_b)c\left(\psi_b^n\right)c(\beta_b) + s\left(\psi_b^n\right)s(\beta_b)}\right), \tag{16}$$

where $\gamma_b \triangleq \theta_b^n - \alpha_b$. The Euler angle derivatives are

$$\begin{bmatrix} \dot{\varphi}_f^n \\ \dot{\theta}_f^n \\ \dot{\psi}_f^n \end{bmatrix} = \begin{bmatrix} 1 & s\left(\varphi_f^n\right)t\left(\theta_f^n\right) & c\left(\varphi_f^n\right)t\left(\theta_f^n\right) \\ 0 & c\left(\varphi_f^n\right) & -s\left(\varphi_f^n\right) \\ 0 & s\left(\varphi_f^n\right)/c\left(\theta_f^n\right) & c\left(\varphi_f^n\right)/c\left(\theta_f^n\right) \end{bmatrix}\boldsymbol{\omega}_{f/n}^f. \tag{17}$$

The angular velocity vector $\boldsymbol{\omega}_{f/n}^f$ is found as in Børhaug and Pettersen (2006):

$$\boldsymbol{\omega}_{f/n}^f = \boldsymbol{\omega}_{b/n}^f + \boldsymbol{\omega}_{f/b}^f = \mathbf{R}_{zy}(\alpha_b, -\beta_b)\boldsymbol{\omega}_{b/n}^b + \boldsymbol{\omega}_{f/b}^f, \tag{18}$$

where $\boldsymbol{\omega}_{b/n}^b = [0, q_b, r_b]^T$ and $\boldsymbol{\omega}_{f/b}^f$ is derived as $\boldsymbol{\omega}_{f/b}^f = [-\dot{\beta}_b \sin(\alpha_b), -\dot{\alpha}_b, \dot{\beta}_b \cos(\alpha_b)]^T$.

To obtain an expression for q_f and r_f as a function of the pitch and yaw rate in b, we insert for $\dot{\alpha}_b$ and $\dot{\beta}_b$ in (18) to obtain

$$\begin{bmatrix} q_f \\ r_f \end{bmatrix} = \mathbf{A}_f \begin{bmatrix} q_b \\ r_b \end{bmatrix} + \mathbf{B}_f, \tag{19}$$

FIGURE 1 The Flow frame variables. To the left is a case with a pure horizontal motion, to the right is a case with pure vertical motion. The axes x^b, y^b, and z^b of the body frame points along u_b, v_b, and w_b, respectively. The Flow frame x^f-axis points along U_b. [Color figure can be viewed at wileyonlinelibrary.com]
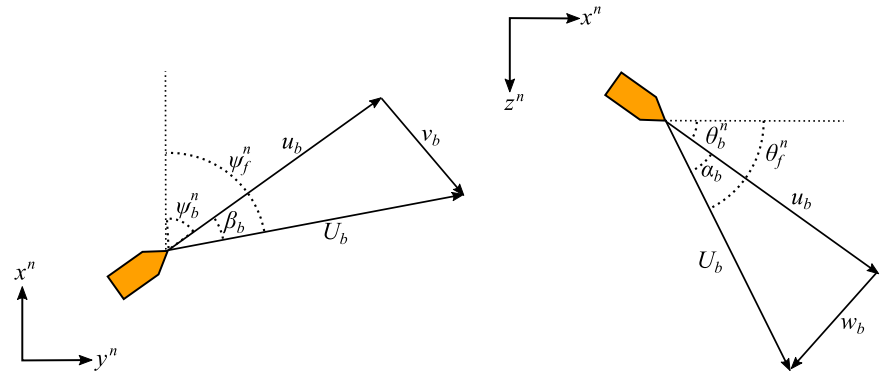
where

$$
A_f \triangleq \begin{bmatrix} c(\beta_b) - \dfrac{X_w u_b}{U_w^2} & -s(\beta_b)s(\alpha_b) \\[2ex] c(\alpha_b)\dfrac{X_w w_b v_b}{U_w U_b^2} & c(\alpha_b)\dfrac{U_w X_v + U_b^2}{U_b^2} \end{bmatrix},
\tag{20}
$$

and

$$
B_f \triangleq \begin{bmatrix} -u_b \dfrac{Z_w s(\theta_b^n) + Y_w w_b}{U_w^2} & v_b c(\alpha_b) \\[2ex] & \dfrac{Z_w s(\theta_b^n) w_b + Y_v U_w^2 + Y_w w_b^2}{U_w U_b^2} \end{bmatrix}^T.
\tag{21}
$$

It can be shown that A_f is nonsingular when the following assumption is met.

Assumption 9. The functions $X_v(u_b)$ and $X_w(u_b)$ satisfy $X_v(u_b) + u_b > 0$ and $-X_w(u_b) + u_b > 0$ for all $u_b \geq u_{\min}$.

This assumption ensures that a change in θ_b^n or ψ_b^n changes θ_f^n or ψ_f^n, respectively, and holds by design for most AUVs operating at maneuvering speed. The expression in (19) enables us to control q_f and r_f, and hence the direction of the vehicle's velocity vector, by controlling the angular rates q_b and r_b of the Body frame.

Remark 2. If the vehicle moves in the horizontal plane without pitch and heave, that is $\alpha_b = \theta_b^n = w_b = 0$, the Flow frame dynamics (19) are reduced to the 2D course dynamics used in Wiig et al. (2019). When pitch and heave are included, however, the dynamic coupling between the Flow frame yaw and pitch adds another layer of complexity to the dynamics. This complexity is removed in the analysis model presented below.

3.4 | Analysis model

The underactuated sway and heave variables introduce dynamic couplings between the yaw and pitch motion in the Flow frame model (19). We would like to remove these $q_b - r_f$ and $r_b - q_f$ couplings to

simplify the analysis in Section 6. The couplings can be removed under the assumption that the angle of attack α_b and sideslip angle β_b are small. Under this assumption, the small angle approximations $c(\alpha_b) \approx 1$, $c(\beta_b) \approx 1$ and $s(\alpha_b)s(\beta_b) \approx 0$ hold. The sideslip angle can then be further simplified as $\beta_b \approx \text{atan2}(v_b, u_b)$, and (19) is reduced to

$$
q_f \approx q_b - \dot{\alpha}_b,
\tag{22a}
$$

$$
r_f \approx r_b + \dot{\beta}_b.
\tag{22b}
$$

The sway and heave dynamics in (10b) and (10c) can then be rewritten in terms of q_f and r_f as

$$
\dot{v}_b \approx \frac{u_b^2 + v_b^2}{X_v u_b + u_b^2 + v_b^2}(X_v r_f + Y_v v_b),
\tag{23a}
$$

$$
\dot{w}_b \approx \frac{U_w^2}{U_w^2 - X_w u_b}(X_w q_f + Y_w w_b + Z_w \sin(\theta_b^n)).
\tag{23b}
$$

The small angle assumption for α_b and β_b holds for vehicles where the hydrodynamic damping and rudder saturation ensures that the turning rate is not too large, which is the case for most AUVs at maneuvering speed.

3.5 | Obstacle and sensing model

The obstacle is modeled as a sphere with radius R_o, with the obstacle frame o at the center. The position and orientation of o with respect to the NED frame is represented by $\eta_o^n \triangleq \left[p_o^n, \theta_o^n, \psi_o^n \right]^T$, where $p_o^n \triangleq [x_o^n, y_o^n, z_o^n]^T$. The obstacle speed is U_o, and the obstacle's angular velocity is $\omega_{o/n}^o \triangleq [q_o, r_o]^T$, where q_o and r_o are the pitch and yaw rate of the obstacle, respectively. Thus, the obstacle model is

$$
\dot{\eta}_o^n = J\left(\eta_o^n\right)\nu_{o/n}^o,
\tag{24a}
$$

$$
\dot{U}_o = a_o,
\tag{24b}
$$

where J is as defined in (4), $\nu_{o/n}^o \triangleq [U_o, 0, 0, q_o, r_o]^T$, and a_o is the obstacle's acceleration. Since the dynamic parameters of the obstacle

can be difficult to estimate, we do not include them in the model. However, we assume that the obstacle's acceleration and angular velocity are smooth and bounded:

Assumption 10. The obstacle's acceleration a_o and angular velocity $\omega_{o/n}^o$ are smooth and bounded by

$$a_o \in [-a_{omax}, a_{omax}], \tag{25a}$$

$$\|\omega_{o/n}^o\| \in [-\omega_{omax}, \omega_{omax}], \tag{25b}$$

where $a_{omax} \geq 0$ and $\omega_{omax} \geq 0$ are constant parameters.

Remark 3. The algorithm can also be applied to nonspherical obstacles. While an analysis of such obstacles is beyond the scope of this paper, the analysis of spherical obstacle avoidance in Section 6 suggests that a limitation on the curvature of the obstacle surface will be required to prove safe avoidance.

To ensure that the vehicle is able to circumvent the obstacle, we need to assume that the obstacle speed is less than the desired vehicle surge speed, u_{bd}. The obstacle speed is further restricted if a large vehicle sway or heave speed is induced toward the obstacle when the vehicle turns away from it, that is if the maneuvering capabilities of the vehicle are poor. This restriction comes from the mathematical analysis in Section 6.

Assumption 11. The obstacle velocity lies in the interval $U_o \in [0, U_{o\,max}]$. The upper bound should satisfy $U_{o\,max} < \min\{U_{omv}, U_{omw}\}$, where

$$U_{omv} < \begin{cases} 2\sqrt{-X_v^2 - X_v u_{bd}}, & -u_{bd} < X_v \leq -\dfrac{u_{bd}}{2}, \\ u_{bd}, & -\dfrac{u_{bd}}{2} < X_v, \end{cases} \tag{26}$$

and

$$U_{omw} < \begin{cases} 2\sqrt{-X_w^2 + X_w u_{bd}}, & \dfrac{u_{bd}}{2} < X_w \leq u_{bd}, \\ u_{bd}, & X_w < \dfrac{u_{bd}}{2}. \end{cases} \tag{27}$$

We require that the vehicle is able to measure the distance $d_o \triangleq \|p_b^n - p_o^n\|$ to the obstacle, as well as the angles to the edge of the obstacle. These angles define a three-dimensional vision cone $\mathcal{V}_o$, which is illustrated in Figure 2. For underwater vehicles, a sensor such as a forward looking sonar can give both d_o and $\mathcal{V}_o$. In addition, we require that the vehicle is able to sense the obstacle velocity, $v_{o/n}^n$, which can either be measured directly using a sensor with Doppler effects, or indirectly using a tracking algorithm.
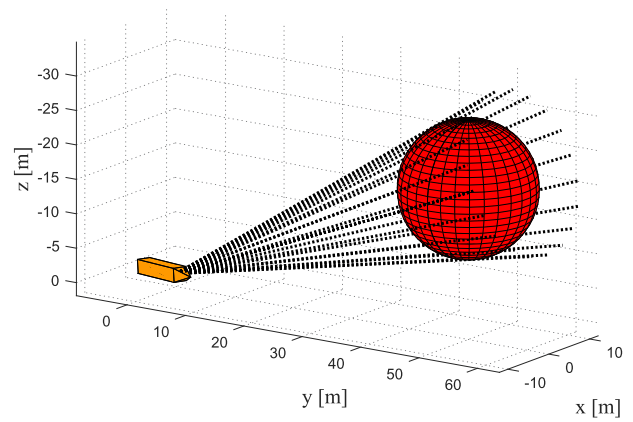

FIGURE 2 A sample of rays (dotted black) creating the vision cone from the vehicle (yellow) to the obstacle (red). [Color figure can be viewed at wileyonlinelibrary.com]

3.6 | Control objectives

The modular nature of the control system presented in this paper makes it possible to implement the proposed collision avoidance algorithm in combination with a variety of nominal guidance laws, such as algorithms for path following, gradient following or adaptive sampling. As the focus in this paper is on the collision avoidance algorithm itself, we will pair it with the simple target reaching guidance law described in Section 4.1. Thus, the goal of the control system is to make the vehicle safely reach a target position p_t^n at some unspecified time $t_f \geq t_0$. We formalize this as

$$\exists\, t_f \in [t_0, \infty) \quad \text{s. t.} \quad \|p_t^{n_b}(t_f)\| \leq d_a, \tag{28}$$

$$d_o(t) \geq d_{safe} > 0 \quad \forall\, t \in [t_0, t_f], \tag{29}$$

where $p_t^{n_b} = p_t^n - p_b^n$ is the target position in n_b, $d_a > 0$ is a user-specified acceptance distance, d_o is the distance to the obstacle and $d_{safe} > 0$ is a design parameter.

Many AUVs have pitch limitations to ensure that they do not move too fast toward the sea floor or the surface, and to keep them within the roll stable regime. For this reason, we require that the control system bounds the pitch of the vehicle in the Flow frame as:

$$\theta_f^n(t) \in [\theta_{fmin}, \theta_{fmax}] \quad \forall\, t \in [t_0, t_f], \tag{30}$$

where $\theta_{fmin} \in (-\pi/2, 0)$ and $\theta_{fmax} \in (0, \pi/2)$ are constant design parameters.

The surge speed u_b will be controlled by using the feedback linearizing controller described in Section 4.4 to reach a desired surge speed u_{bd}. In this paper, we set the desired surge speed to a positive constant:

Assumption 12. The desired surge speed is constant and satisfies $u_{bd} \geq u_{min}$.

For brevity, we introduce the notation $X_{vd} \triangleq X_v(u_{bd})$, $Y_{vd} \triangleq Y_v(u_{bd})$, $X_{wd} \triangleq X_w(u_{bd})$, and $Y_{wd} \triangleq Y_w(u_{bd})$.

4 | CONTROL SYSTEM

When no obstacles are at risk of collision with the vehicle, the vehicle will be in guidance mode and under the control of a target reaching guidance law described in this section. If there is a risk of collision, the control system will enter into collision avoidance mode according to a rule we will give in Section 5.3. The vehicle will then be under the control of the proposed collision avoidance algorithm, which is described in Section 5.

In this section we also describe the controllers used to steer the Flow frame of the vehicle, as well as the low level yaw rate, pitch rate, and surge controllers.

4.1 | Target reaching guidance law

We will employ a pure pursuit guidance law (Breivik & Fossen, 2008) to make the vehicle reach the target position $\boldsymbol{p}_t^n$. The desired heading ψ_{dg}^n is thus set to point toward the target:

$$\psi_{dg}^n \triangleq \Psi\left(\boldsymbol{p}_t^{nb}\right), \tag{31}$$

where Ψ is defined in (1).

The desired pitch θ_{dg}^n in guidance mode is saturated to ensure that control objective (30) is met:

$$\theta_{dg}^n = \begin{cases} \theta_{fmax}, & \Theta\left(\boldsymbol{p}_t^{nb}\right) > \theta_{fmax}, \\ \Theta\left(\boldsymbol{p}_t^{nb}\right), & \Theta\left(\boldsymbol{p}_t^{nb}\right) \in [\theta_{fmin}, \theta_{fmax}], \\ \theta_{fmin}, & \Theta\left(\boldsymbol{p}_t^{nb}\right) < \theta_{fmin}, \end{cases} \tag{32}$$

where Θ is defined in (2).

The desired velocity vector in guidance mode, $\boldsymbol{v}_{dg}^{nb}$, is then found from the guidance laws (31) and (32) as:

$$\boldsymbol{v}_{dg}^{nb} \triangleq \boldsymbol{R}_{zy}\left(\theta_{dg}^n, \psi_{dg}^n\right)[U_b \quad 0 \quad 0]^T. \tag{33}$$

4.2 | Flow frame control

To account for the underactuated dynamics, we will steer the direction of the vehicle's velocity vector, that is we will control $\dot{\theta}_f^n$ and $\dot{\psi}_f^n$. To this end, we use (19) to obtain

$$\begin{bmatrix} \bar{q}_{bd} \\ \bar{r}_{bd} \end{bmatrix} = \boldsymbol{A}_f^{-1}\left(\begin{bmatrix} q_{fd} \\ r_{fd} \end{bmatrix} - \boldsymbol{B}_f\right). \tag{34}$$

The desired Flow frame angular rates q_{fd} and r_{fd} are obtained as

$$q_{fd} = c\left(\varphi_f^n\right)\dot{\theta}_{fc}^n + c\left(\theta_f^n\right)s\left(\varphi_f^n\right)\dot{\psi}_{fc}^n, \tag{35}$$

$$r_{fd} = -s\left(\varphi_f^n\right)\dot{\theta}_{fc}^n + c\left(\theta_f^n\right)c\left(\varphi_f^n\right)\dot{\psi}_{fc}^n. \tag{36}$$

The signals $\dot{\theta}_{fc}^n$ and $\dot{\psi}_{fc}^n$ are set using a proportional controller to obtain exponential convergence of the Flow frame heading and pitch. To limit the yaw and pitch rate, and hence the induced sway and heave motions, the proportional effect is saturated (Wiig et al., 2019):

$$\dot{\psi}_{fc}^n \triangleq \dot{\psi}_{fd}^n - \text{sat}(k_\psi \tilde{\psi}_f^n, \sigma_\psi), \tag{37a}$$

$$\dot{\theta}_{fc}^n \triangleq \dot{\theta}_{fd}^n - \text{sat}(k_\theta \tilde{\theta}_f^n, \sigma_\theta), \tag{37b}$$

where $\tilde{\theta}_f^n \triangleq \theta_f^n - \theta_{fd}^n$ and $\tilde{\psi}_f^n \triangleq \psi_f^n - \psi_{fd}^n$. We define these error variables to lie in the interval $(-\pi, \pi]$ to ensure that the vehicle makes the shortest turn toward ψ_{fd}^n and θ_{fd}^n. The desired heading ψ_{fd}^n and pitch θ_{fd}^n are given in Section 4.1 when the control system is in guidance mode, and in Section 5 when the control system is in collision avoidance mode. The control gains $k_\psi > 0$ and $k_\theta > 0$ are positive design variables, while the variables $\sigma_\psi > 0$ and $\sigma_\theta > 0$ are saturation parameters used in the saturation function

$$\text{sat}(a, b) \triangleq \begin{cases} b, & a > b, \\ a, & a \in [-b, b], \\ -b, & a < -b. \end{cases} \tag{38}$$

To ensure that the Flow frame heading saturation acts on an error in the interval $\tilde{\psi}_f^n \in (-\pi, \pi]$, we make the following assumption on σ_ψ:

Assumption 13.

$$\sigma_\psi < k_\psi \pi. \tag{39}$$

Similarly, to ensure that the Flow frame pitch rate saturation acts on an error in the interval $\tilde{\theta}_f^n \in (-\pi/2, \pi/2)$ we assume that:

Assumption 14.

$$\sigma_\theta < k_\theta \frac{\pi}{2}. \tag{40}$$

Remark 4. If Assumptions 13 and 14 are not met, the saturation will not have any effect and can be removed.

Remark 5. The proposed Flow frame controller enables both the collision avoidance law proposed in Section 5 and the nominal guidance law presented in Section 4.1 to steer the vehicle using only the desired velocity direction. Thus, these algorithms can also be applied to vehicles with different dynamics, such as quadcopters, provided a vehicle velocity controller is available.

4.3 | Yaw and pitch rate bump function

When the control system switches mode, there is a discontinuity in ψ_{fd}^n and θ_{fd}^n, and hence in $\bar{r}_{bd}$ and $\bar{q}_{bd}$. To avoid the discontinuity in the desired yaw and heading rate, we introduce a C^1 function BUMP(t_b):

$$\text{BUMP}(t_b) = \begin{cases} 1, & t_b \geq T_b, \\ \left(1 - \cos\left(\frac{\pi t_b}{T_b}\right)\right)/2, & 0 < t_b < T_b, \\ 0, & t_b \leq 0, \end{cases} \quad (41)$$

where the bump time T_b is a positive constant.

As long as the yaw rate signal $\bar{r}_{bd}$ from (34) is smooth, $r_{bd} = \bar{r}_{bd}$. However, if there is a jump in $\bar{r}_{bd}$ at time t_1, we apply the bump function:

$$r_{bd}(t) = r_{bd}(t_1)[1 - \text{BUMP}(t - t_1)] + \bar{r}_{bd}(t)\text{BUMP}(t - t_1). \quad (42)$$

This ensures that when $t \geq t_1 + T_b$, $r_{bd}(t) = \bar{r}_{bd}(t)$. The pitch rate signal $\bar{q}_{bd}$ is smoothed in the same way.

4.4 | Low level controllers

The surge (10a), pitch rate and yaw rate (10e) are controlled using feedback linearizing controllers like the one described in Caharija et al. (2016):

$$\tau_u = -F_{u_b}(\theta_b^n, u_b, v_b, w_b, r_b, q_b) + \dot{u}_{bd} - k_u \tilde{u}_b, \quad (43a)$$

$$\tau_q = -F_{q_b}\left(\theta_b^n, u_b, w_b, q_b\right) + \dot{q}_{bd} - k_q \tilde{q}_b, \quad (43b)$$

$$\tau_r = -F_{r_b}(u_b, v_b, r_b) + \dot{r}_{bd} - k_r \tilde{r}_b, \quad (43c)$$

where $k_u > 0, k_q > 0$, and $k_r > 0$ are constant control gains, and $\tilde{u}_b \triangleq u_b - u_{bd}, \tilde{q}_b \triangleq q_b - q_{bd}$, and $\tilde{r}_b \triangleq r_b - r_{bd}$.

Inserting these controllers into (10a) and (10e) gives the following error dynamics:

$$\dot{\tilde{u}}_b = -k_u \tilde{u}_b, \quad (44a)$$

$$\dot{\tilde{q}}_b = -k_q \tilde{q}_b, \quad (44b)$$

$$\dot{\tilde{r}}_b = -k_r \tilde{r}_b. \quad (44c)$$

The error dynamics are linear, and the origin is globally exponentially stable. Hence, as long as q_{bd}, r_{bd}, and u_{bd} are continuous signals, a vehicle described by (10) will be able to follow them as long as the following assumption is met:

Assumption 15. At time t_0, the system has operated long enough for the surge speed, yaw rate, and pitch rate to converge, that is $\tilde{u}_b(t_0) = 0, \tilde{q}_b(t_0) = 0$, and $\tilde{r}_b(t_0) = 0$.

Remark 6. To fulfill this assumption, the vehicle needs to be properly initialized before control is handed over to the automatic collision avoidance system, which is reasonable.

5 | COLLISION AVOIDANCE ALGORITHM

In this section we will present the proposed collision avoidance law, the constant avoidance angle algorithm. The algorithm consists of three components; the creation of a motion compensated vision cone V_c (Section 5.1), choosing a direction among the rays of V_c (Section 5.2), and a rule for entering and leaving collision avoidance mode (Section 5.3). In addition, we provide a brief description in Section 5.4 of how to extend the algorithm to handle multiple obstacles.

5.1 | Creating the motion compensated vision cone

To get a cone from the vehicle to the obstacle, where each ray has an avoidance angle $\alpha_o \in [0, \pi/2)$ to the obstacle, the vision cone $\mathcal{V}_o$ is extended to a cone $\mathcal{V}_e$ as illustrated in Figure 3. In the case of a spherical obstacle, an analytical expression for the apex angle of $\mathcal{V}_o$ is $2\gamma_a$, where

$$\gamma_a \triangleq \sin^{-1}\left(\frac{R_o}{R_o + d_o}\right). \quad (45)$$

The apex angle of $\mathcal{V}_e$ is then $\gamma_e \triangleq 2(\gamma_a + \alpha_o)$.

Remark 7. If the obstacle is not spherical, each ray of the vision cone $\mathcal{V}_o$ is rotated α_o radians in the direction normal to the obstacle surface to obtain $\mathcal{V}_e$.

In the case of a static obstacle, any direction along $\mathcal{V}_e$ will maintain the avoidance angle α_o to the obstacle, and thus avoid it. If the
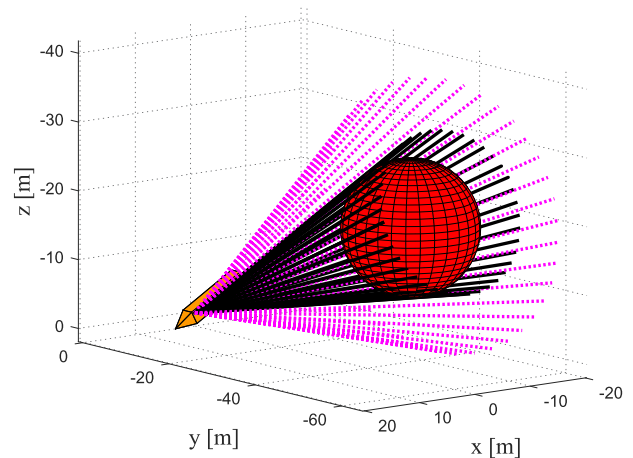

FIGURE 3 The vision cone $\mathcal{V}_o$ (black) and the extended vision cone $\mathcal{V}_e$ (dotted magenta). [Color figure can be viewed at wileyonlinelibrary.com]

obstacle is moving, we will perform a transformation of $\mathcal{V}_e$ to compensate for the obstacle movement. This transformation ensures that when the resulting cone is observed through a nonrotating co-ordinate frame moving with the obstacle, each ray will still keep the constant avoidance angle to the obstacle edge.

To compensate a ray ρ for the obstacle velocity, we will find a frame F_ρ which is such that the x^{F_ρ}-axis points along ρ, while the obstacle velocity vector lies in the x^{F_ρ}–y^{F_ρ}-plane. We start by defining an intermediate frame A, where the x^A-axis is coincident with the x^{F_ρ}-axis. We will then find a rotation from the A frame to the F_ρ frame.

The A frame is obtained in two steps. First we do a rotation from the n_b frame to the b_{vo} frame, which is a Body-fixed frame with the x-axis pointing from the vehicle to the obstacle: $\boldsymbol{R}_{n_b}^{b_{vo}} \triangleq \boldsymbol{R}_{zy}(\Theta(\boldsymbol{p}_o^{n_b}), \Psi(\boldsymbol{p}_o^{n_b}))^T$. We then do a rotation from the b_{vo} frame to the A frame using a rotation of ϕ radians around the $x^{b_{vo}}$-axis, followed by a rotation of γ_e radians around the resulting z-axis, $\boldsymbol{R}_{b_{vo}}^A \triangleq \boldsymbol{R}_z(\gamma_e)^T \boldsymbol{R}_x(\phi)^T$. The angle ϕ thus becomes a parameter which can uniquely identify each ray of the vision cone.

The obstacle velocity in the A frame is $\boldsymbol{v}_o^A = \boldsymbol{R}_{n_b}^A \boldsymbol{v}_{o/n}^n$. To obtain the frame F_ρ, we will rotate the A frame around the x^A-axis until $\boldsymbol{v}_o^{F_\rho}$ lies in the x^{F_ρ}–y^{F_ρ}-plane. The required rotation angle can be geometrically found as $\hat{\phi} \triangleq \text{atan2}(v_{o,z}^A, v_{o,y}^A)$. Hence, $\boldsymbol{R}_A^{F_\rho} = \boldsymbol{R}_x(\hat{\phi})$, and

$$\boldsymbol{v}_o^{F_\rho} = \boldsymbol{R}_{n_b}^{F_\rho} \boldsymbol{v}_{o/n}^n = \boldsymbol{R}_A^{F_\rho} \boldsymbol{R}_{b_{vo}}^A \boldsymbol{R}_{n_b}^{b_{vo}} \boldsymbol{v}_{o/n}^n. \quad (46)$$

We are now ready to perform the motion compensation. We define a velocity vector $\boldsymbol{v}_\rho^{F_\rho}$ along ρ. We seek a vector $\boldsymbol{v}_{ca,\rho}^{F_\rho}$ which is such that $\boldsymbol{v}_\rho^{F_\rho} + \boldsymbol{v}_o^{F_\rho} = \boldsymbol{v}_{ca,\rho}^{F_\rho}$, that is we compensate the vector $\boldsymbol{v}_\rho^{F_\rho}$ for the obstacle velocity. This is illustrated in Figure 4. The vector $\boldsymbol{v}_{ca,\rho}^{F_\rho}$ is a possible desired velocity from the collision avoidance algorithm. Hence, we would like to specify its magnitude, in particular we
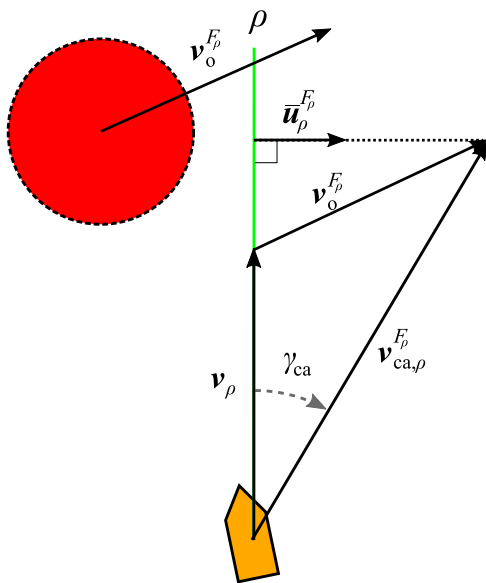
require that $\|\boldsymbol{v}_{ca,\rho}^{F_\rho}\| = U_b$, where U_b is the total velocity speed $\|\boldsymbol{v}_{b/n}^b\|$ as defined in Section 3.3. We do this by finding the angle γ_{ca} between $\boldsymbol{v}_\rho^{F_\rho}$ and $\boldsymbol{v}_{ca,\rho}^{F_\rho}$, which is given by

$$\gamma_{ca}(\phi) \triangleq \sin^{-1}\left(\frac{\left(\boldsymbol{v}_o^{F_\rho}\right)^T \bar{\boldsymbol{u}}_\rho^{F_\rho}}{U_b} \right), \quad (47)$$

where $\bar{\boldsymbol{u}}_\rho^{F_\rho}$ is a unit vector orthogonal to $\boldsymbol{v}_\rho^{F_\rho}$ as shown in Figure 4. The expression for γ_{ca} is ensured to be well defined by Assumption 11. The vector $\boldsymbol{v}_{ca,\rho}^{F_\rho}$ is thus given by

$$\boldsymbol{v}_{ca,\rho}^{F_\rho} \triangleq U_b [\cos(\gamma_{ca}), \sin(\gamma_{ca}), 0]^T, \quad (48)$$

while

$$\boldsymbol{v}_{ca,\rho}^n = \left(\boldsymbol{R}_{n_b}^{F_\rho}\right)^T \boldsymbol{v}_{ca,\rho}^{F_\rho}. \quad (49)$$

The velocity direction required to follow a motion compensation ray is defined by

$$\psi_\rho^n(\phi) \triangleq \Psi\left(\boldsymbol{v}_{ca,\rho}^n(\phi)\right), \quad (50a)$$

$$\theta_\rho^n(\phi) \triangleq \Theta\left(\boldsymbol{v}_{ca,\rho}^n(\phi)\right). \quad (50b)$$

The collection of motion compensated rays composes the motion compensated vision cone V_c, which is shown in Figure 5. The desired heading and pitch angle in collision avoidance are chosen by minimizing a cost function $C(\phi)$. Thus, if $\phi_{ca} \triangleq \arg\min_\phi C(\boldsymbol{e}_\rho(\phi))$, we obtain the desired heading and pitch angle in collision avoidance as

$$\left\langle \theta_{dca}^n, \psi_{dca}^n \right\rangle \triangleq \left\langle \theta_\rho^n(\phi_{ca}), \psi_\rho^n(\phi_{ca}) \right\rangle. \quad (51)$$

Equation (51) forms the core of the collision avoidance law presented in this paper. Even though there are several steps leading up to
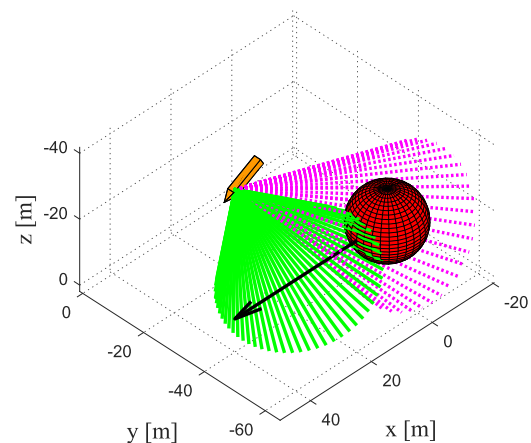

FIGURE 4 A plane containing both the ray ρ, the obstacle velocity vector $\boldsymbol{v}_{o/n}^n$ and the resulting candidate for desired velocity in collision avoidance mode, $\boldsymbol{v}_{ca,\rho}^n$. [Color figure can be viewed at wileyonlinelibrary.com]

FIGURE 5 The extended vision cone $\mathcal{V}_e$ (dotted magenta) is compensated for the velocity of the obstacle (black arrow) to create the compensated vision cone V_c (solid green). [Color figure can be viewed at wileyonlinelibrary.com]

this expression, they are straight forward to implement and are based on measurements that are readily available on most platforms. We will now provide an example for the cost function $C(\phi)$.

Remark 8. If both the obstacle and vehicle is moving in the horizontal plane without pitching, the collection of motion compensated rays (50) reduces to one ray on the port side and one ray on the starboard side of the obstacle, which is equivalent to the 2D algorithm proposed in Wiig et al. (2019). The motion compensation has a higher level of complexity in 3D, as shown in the derivation of (50), which gives the benefit of providing a larger solution space for finding a collision avoidance maneuver, as described below.

5.2 | Choosing a safe direction

When the vehicle enters collision avoidance mode, any direction along V_c is a safe candidate for collision avoidance. This provides flexibility, and a ray can, for example, be chosen to minimize the angular distance to a safe direction, or to satisfy some external rules of the road. In this paper, we will make the vehicle move behind the obstacle, which we do by maximizing the angular distance from the obstacle's velocity vector to the chosen ray. We thus seek to minimize the cost function C_{v_o}, defined as

$$C_{v_o} \triangleq -\sqrt{\left(\theta_o^n - \theta_\rho^n\right)^2 + \left(\psi_o^n - \psi_\rho^n\right)^2}. \tag{52}$$

To ensure that θ_f^n stays within the required limits (30), we add the following cost function:

$$C_\theta \triangleq 2\pi\left(1 + \tanh\left(\lambda\left[\theta_{fmin} - \theta_\rho^n\right]\right)\right)$$
$$+ 2\pi\left(1 + \tanh\left(\lambda\left[\theta_\rho^n - \theta_{fmax}\right]\right)\right), \tag{53}$$

where $\lambda > 0$ is a design parameter used to set the slope of C_θ. The smoothness of C_θ ensures the smoothness of $\dot{\theta}_{dca}^n$ during the collision avoidance maneuver. An example C_θ is shown in Figure 6, where $\theta_{min} = -0.2$, $\theta_{max} = 0.4$, and $\lambda = 50$.

When the control system is already in collision avoidance mode, we will avoid discontinuities in θ_{dca}^n and ψ_{dca}^n by minimizing the change in desired heading and pitch when choosing a ray:

$$C_{qr} \triangleq \sqrt{\left(\theta_{dca}^n - \theta_{dca1}^n\right)^2 + \left(\psi_{dca}^n - \psi_{dca1}^n\right)^2}, \tag{54}$$

where θ_{dca1}^n and ψ_{dca1}^n is the desired pitch and heading during the previous optimization, respectively. Thus, if the system enters collision avoidance mode at a time t_1, the cost function C becomes

$$C \triangleq \begin{cases} C_{v_o} + C_\theta, & t = t_1, \\ C_{qr} + C_\theta, & t > t_1. \end{cases} \tag{55}$$

5.3 | Switching rule

We define that the vehicle enters CA mode at a time t_1 if the distance $d_o(t_1)$ to the obstacle is less than or equal to a chosen distance d_{switch}, and the desired velocity vector $v_{dg}^{nb}(t_1)$ (33) from the nominal guidance laws (31) and (32) is within the extended vision cone $\mathcal{V}_e(t_1)$:

$$v_{dg}^{nb}(t_1) \in \mathcal{V}_e(t_1), \tag{56a}$$

$$d_o(t_1) \leq d_{switch} > d_{safe}. \tag{56b}$$

Nominal guidance towards the target will resume at a time t_2 when $v_{dg}^{nb}(t_2)$ moves outside $\mathcal{V}_e(t_2)$:

$$v_{dg}^{nb}(t_2) \notin \mathcal{V}_e(t_2). \tag{57}$$

5.4 | Multiple obstacles

The constant avoidance angle algorithm can be extended to multiobstacle scenarios. In such scenarios, there will be multiple vision cones, which may be overlapping. The overlapping cones will be merged, so that only the outermost rays of the cones are considered. Then, a safe ray can be chosen in the same manner as for a single obstacle scenario.

If the vehicle encounters a new obstacle while already in collision avoidance mode, we need to ensure that the direction minimizing (55) when the new obstacle is included does not make the vehicle maneuver in front of or into any of the previous obstacles. We achieve this by making the vehicle maintain a constant horizontal turning direction, like in the two dimensional case in Wiig et al. (2019). Thus, if the vehicle starts an avoidance maneuver by going around the obstacles in a clockwise fashion, it will continue to do so until the avoidance maneuver is completed.

While the detailed analysis of a multiobstacle scenario is beyond the scope of this paper, we have included simulations with multiple obstacles in Section 7.2 to demonstrate the applicability to such scenarios.
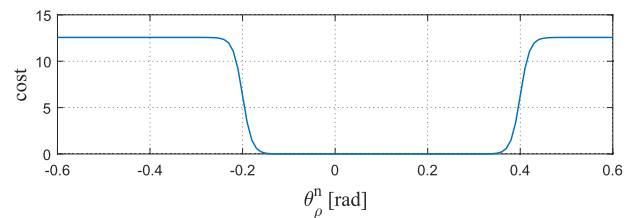

FIGURE 6 The cost function C_θ when $\theta_{min} = -0.2$, $\theta_{max} = 0.4$, and $\lambda = 50$. [Color figure can be viewed at wileyonlinelibrary.com]

6 | ANALYSIS

In this section, we provide an analysis of the constant avoidance angle algorithm presented in Section 5, which we apply to an underactuated marine vehicle modeled as in Section 3.2. The algorithm will provide heading and pitch references to the Flow frame controller in Section 4.2, which again will provide references to the yaw and pitch rate controller in Section 4.4. When the vehicle is not in collision avoidance mode, it is in nominal guidance mode, employing the pure pursuit guidance law described in Section 4.1 to steer it toward a target position.

We will first give a lower bound on the minimum distance obtained between the vehicle and the obstacle when the vehicle keeps a constant avoidance angle α_o to the obstacle. We then show how we can bound the sway and heave speed during the maneuver, and demonstrate how we can use these bounds as design parameters to ensure a maneuver that is feasible, well defined and safe. These bounds are used to find a minimum switching distance, ensuring that the vehicle is able to safely enter collision avoidance mode. Finally, we use these results to derive conditions under which the vehicle is mathematically guaranteed to reach the target without collisions.

For this section, we assume that the obstacles are sparsely spaced, ensuring that the vehicle will only have to avoid one obstacle at a time:

Assumption 16. The distance between two obstacles are always at least $2d_{switch}$.

We will also employ the notation $X_{vd} \triangleq X_v(u_{bd})$, $Y_{vd} \triangleq Y_v(u_{bd})$, $X_{wd} \triangleq X_w(u_{bd})$, and $Y_{wd} \triangleq Y_w(u_{bd})$ as defined in Section 3.6.

6.1 | Lower bound on the avoidance angle

To ensure that the vehicle stays at least a minimum safety distance d_{safe} away from the obstacle during the collision avoidance maneuver, the avoidance angle α_o needs to be lower bounded.

Lemma 1. If the obstacle is static, the vehicle's velocity vector maintains an avoidance angle α_o to the obstacle for $t \geq t_0$, the initial obstacle distance satisfies $d_o(t_0) \geq d_{safe}$ and α_o satisfies

$$\alpha_o \geq \cos^{-1}\left(\frac{R_o}{R_o + d_{safe}}\right), \tag{58}$$

then $d_o(t) \geq d_{safe}$ for all $t \geq t_0$.

Proof. When the angle between vision cone from the vehicle to the obstacle and the vehicles's velocity vector is α_o, $\dot{d}_o$ can be found as:

$$\dot{d}_o = -U_b \cos(\gamma_a(t) + \alpha_o). \tag{59}$$

Equation (59) has an equilibrium point at $\gamma_a(t) = \pi/2 - \alpha_o$, which occurs when

$$d_o(t) = d_{omin} \triangleq \frac{R_o}{\cos(\alpha_o)} - R_o. \tag{60}$$

Furthermore, when $d_o(t) < d_{omin}$, $\dot{d}_o(t) > 0$, while when $d_o(t) > d_{omin}$, $\dot{d}_o(t) < 0$. It follows that if $d_{safe} = d_{omin}$, $d_o(t_0) \geq d_{safe}$, and the avoidance angle satisfies (58), then a vehicle maintaining the avoidance angle α_o will not get closer than d_{safe} to the obstacle. ☐

6.2 | Limiting sway and heave

In this section, we will provide a lower bound on the safety distance d_{safe} and upper bounds on the Flow frame control saturation parameters σ_ψ and σ_θ to ensure that the sway and heave motions are bounded by v_{bsup} and w_{bsup}, respectively. The required control effort in heading and pitch is maximized if the entire avoidance maneuver is made in either the horizontal or vertical plane, and if the obstacle moves in the same plane. Thus, even though the use of the cost function (55) combines a yaw and pitch movement to minimize the control effort required in each DOF, we will examine a pure pitch and a pure yaw maneuver to determine the bounds on the control parameters.

The desired Flow frame angular rates during collision avoidance is dependent on v_b and w_b. In the next Lemma, we will utilize the analysis model (22a)–(23b) to derive a requirement on this dependency which ensures that v_b and w_b remain bounded:

Lemma 2. Let the sway and heave velocities be modeled by (23a) and (23b). Suppose that the Flow frame pitch rate q_f and yaw rate r_f are functions of the sway and heave motions, respectively, in such a way that:

$$|q_f(w_{bsup})| < \frac{|Y_{wd}|}{|X_{wd}|}w_{bsup} - \frac{|Z_w|}{|X_{wd}|}, \tag{61}$$

$$|r_f(v_{bsup})| < \frac{|Y_{vd}|}{|X_{vd}|}v_{bsup}, \tag{62}$$

where $v_{bsup} > 0$ and

$$w_{bsup} > \frac{|Z_w|}{|Y_{wd}|}. \tag{63}$$

Then, if Assumption 15 holds, $v_b(t_0) < v_{bsup}$ and $w_b(t_0) < w_{bsup}$,

$$v_b(t) < v_{bsup} \quad \forall t \geq t_0, \tag{64}$$

$$w_b(t) < w_{bsup} \quad \forall t \geq t_0. \tag{65}$$

Proof. Consider the Lyapunov function candidate $V(w_b) = 0.5w_b^2$ of (23b) with time derivative

$$\dot{V} = \frac{U_w^2}{U_w^2 - X_{wd}u_b}\left(X_{wd}w_b q_f(w_b) + Y_{wd}w_b^2 + Z_w \sin(\theta_b^n)w_b\right). \tag{66}$$

Using Assumption 8 we can upper bound $\dot{V}$ as

$$\dot{V} \leq \frac{U_w^2}{U_w^2 - X_{wd}u_b}(|X_{wd}||w_b||q_f(w_b)| - |Y_{wd}|\,w_b^2 + |Z_w||w_b|). \quad (67)$$

Inserting for (61), we obtain that $\dot{V} \leq 0$ on a set

$$\Omega_V \triangleq \left\{w_b \in \mathbb{R} \,|\, V \leq \frac{1}{2}w_{bsup}^2\right\}, \quad (68)$$

which is a level set of V with $w_b = w_{bsup}$ on the boundary. Hence, the set Ω_V is positively invariant, and any solution of w_b starting in Ω_V cannot leave it, which proves the that bound (65) holds. The proof for the bound (64) on v_b is equivalent. $\qquad\square$

Remark 9. The lower bound on w_{bsup} in (63) stems from the effect of gravity. Specifically, when $\theta_b^n \neq 0$, a pitch moment is induced around CB. The distance between CB and b makes part of this moment into an acceleration in heave, which is reflected in (63).

We are now ready to derive bounds on the Flow frame controllers (37) and on the minimum safety distance d_{safe} which ensures that (61) and (62) are satisfied. We do this in the next two lemmas, which consider a pure vertical and a pure horizontal maneuver. These results will then be combined in Theorem 1. In the next Lemma, we will use the following term:

$$F_\theta \triangleq \frac{w_{bsup}|Y_{wd}| - |Z_w|}{|X_{wd}|} - \frac{2w_{bsup}^2|Y_{wd}|\,U_{o\,max}}{\left(U_{wsup}^2 - X_{wd}u_b\right)\sqrt{U_{wsup}^2 - U_{o\,max}^2}}$$
$$- \omega_{o\,max}\frac{U_{o\,max}}{u_b} - \frac{a_{o\,max}}{\sqrt{u_b^2 - U_{o\,max}^2}}, \quad (69)$$

where $U_{wsup} \triangleq \sqrt{u_b^2 + w_{bsup}^2}$.

Lemma 3. *Consider a vehicle and an obstacle moving in the same vertical plane. Let the vehicle kinematics be modeled by (5), the actuated surge, pitch, and yaw dynamics be modeled by (10a), (10d), and (10e), and the underactuated sway and heave dynamics be modeled by (23a)–(23b). Let the vehicle be governed by the surge controller (43a), pitch rate controller (43b), and the Flow frame pitch controller (37b). Let the control system enter collision avoidance mode at time t_1, and let the vehicle Flow frame then be steered by the constant avoidance angle algorithm in Section 5.1. Define a parameter $\kappa_\theta \in (0, 1)$, and assume that the distance between the vehicle and the obstacle satisfies $d_o(t) > d_{safe} \quad \forall\, t \geq t_1$. If Assumptions 8–12 and 15–16 hold, the Flow frame proportional saturation σ_θ satisfies*

$$\sigma_\theta \leq \kappa_\theta F_\theta, \quad (70)$$

the safety distance d_{safe} satisfies

$$d_{safe} \geq \frac{(U_{wsup} + U_{o\,max})^2}{U_{wsup}} \frac{1}{(1 - \kappa_\theta)F_\theta}, \quad (71)$$

and the heave motion satisfies $|w_b(t_0)| < w_{bsup}$, where

$$w_{bsup} \geq \frac{|Z_w|}{|Y_{wd}|}, \quad (72)$$

then

$$|w_b(t)| < w_{bsup} \quad \forall\, t \geq t_0. \quad (73)$$

Proof. The proof of Lemma 3 includes the gravity restoration term Z_w, but otherwise follows along the lines of Wiig et al. (2019). The lemma is proved by finding an upper bound on q_{fd} for a given w_{bsup}. The upper bound is inserted into (61), which allows us to apply Lemma 2. We then obtain (70) and (71) by solving for σ_θ and d_{safe}.

Without loss of generality, we assume that the maneuver is made by moving above the obstacle. Furthermore, since there is no horizontal movement or turning, we allow the pitch angles of the vehicle and the obstacle to lie in the interval $(-\pi, \pi]$. Thus, the vehicle and the obstacle can move toward each other while keeping the same heading. The collision avoidance geometry in the x–z-plane is shown in Figure 7. The time derivative of θ_{dca}^n is

$$\dot{\theta}_{dca}^n = \dot{\theta}_{\alpha_o}^n + \dot{\gamma}_{ca}. \quad (74)$$

As shown in Figure 7, the angle $\theta_{\alpha_o}^n$ can be decomposed into

$$\theta_{\alpha_o}^n = \gamma_o + \gamma_a + \alpha_o. \quad (75)$$

Hence,

$$\dot{\theta}_{\alpha_o}^n = \dot{\gamma}_o + \dot{\gamma}_a. \quad (76)$$

The angular rate $\dot{\gamma}_o$ can be found geometrically as

$$\dot{\gamma}_o = \frac{U_o \sin\left(\theta_o^n - \gamma_o\right) - U_b \sin\left(\theta_f^n - \gamma_o\right)}{R_o + d_o}, \quad (77)$$

while $\dot{\gamma}_a$ is found as

$$\dot{\gamma}_a = -\dot{d}_o\frac{R_o}{(R_o + d_o)\sqrt{(R_o + d_o)^2 - R_o^2}}, \quad (78)$$

where

$$\dot{d}_o = U_o \cos\left(\theta_o^n - \gamma_o\right) - U_b \cos\left(\theta_f^n - \gamma_o\right). \quad (79)$$

Combining (77)–(79) gives

$$\dot{\theta}_{\alpha_o}^n = \frac{U_b \sin\left(\gamma_o - \theta_f^n\right) - U_o \sin\left(\gamma_o - \theta_f^n\right)}{R_o + d_o}$$
$$- R_o\frac{U_b \cos\left(\gamma_o - \theta_f^n\right) - U_o \cos\left(\gamma_o - \theta_o^n\right)}{(R_o + d_o)\sqrt{d_o(2R_o + d_o)}}. \quad (80)$$

When both the vehicle and the obstacle moves in the same vertical plane, the dot product $\left(v_o^{F_\rho}\right)^T \bar{u}_\rho^{F_\rho}$ can be rewritten as $U_o \sin(\gamma_{vo})$, where

$$\gamma_{vo} \triangleq \pi - \left(\theta_o^n - \theta_{\alpha o}^n\right), \tag{81}$$

The expression (47) for γ_{ca} can then be rewritten as

$$\gamma_{ca} = \sin^{-1}\left(\frac{U_o \sin(\gamma_{vo})}{U_b}\right), \tag{82}$$

where we in effect have used the sine rule on the triangle shown in Figure 8. We use (82) to find

$$\dot{\gamma}_{ca} = \frac{U_o\left(\cos(\gamma_{vo})\left(\dot{\theta}_{\alpha o}^n - q_o\right) + \sin(\gamma_{vo})\left(\frac{a_o}{U_o} - \frac{\dot{U}_b}{U_b}\right)\right)}{\sqrt{U_b^2 - U_o^2 \sin^2(\gamma_{vo})}}. \tag{83}$$

The total vehicle acceleration $\dot{U}_b$ is found as

$$\dot{U}_b = U_b w_b \frac{X_{wd} q_f + Y_{wd} w_b}{U_b^2 - X_{wd} u_b}, \tag{84}$$

where we have used the fact that $\dot{u}_b = \dot{u}_{bd}$ by Assumption 15, and that $\dot{u}_{bd} = 0$ by Assumption 12.

Note that $\dot{\theta}_{dca}^n$ depends on q_{fd}, which again depends on $\dot{\theta}_{dca}^n$ when the control system is in collision avoidance mode. A closed expression for q_{fd} is found by inserting (74) into the Flow frame pitch control law (37b), which gives

$$q_{fd}(w_b) = \frac{G_{num}(w_b)}{G_{den}(w_b)}, \tag{85}$$

where

$$G_{num} \triangleq \dot{\theta}_{\alpha o}^n + \frac{U_o \cos(\gamma_{vo})\left(\dot{\theta}_{\alpha o}^n - q_o\right) + \sin(\gamma_{vo})\left(a_o - \frac{U_o Y_{wd} w_b^2}{U_b^2 + X_{wd} u_b}\right)}{\sqrt{U_b^2 - U_o^2 \sin^2(\gamma_{vo})}} - \text{sat}\left(k_\theta \tilde{\theta}_f^n\right), \tag{86}$$

and

$$G_{den} \triangleq 1 + \frac{U_o \sin(\gamma_{vo}) w_b X_{wd}}{\sqrt{U_b^2 - U_o^2 \sin^2(\gamma_{vo})}\left(U_b^2 - X_{wd} u_b\right)}. \tag{87}$$

The expression for (87) is ensured to be well defined by Assumptions 9 and 11. However, to ensure that q_{fd} in (85) is well defined, we require that $G_{den} > 0$. We obtain a lower bound on (87) by minimizing with respect to γ_{vo} and w_b:

$$G_{den} > 1 - \frac{U_{o\max}|w_b||X_{wd}|}{\left(U_b^2 - X_{wd} u_b\right)\sqrt{U_b^2 - U_{o\max}^2}} := G_{dinf}(w_b). \tag{88}$$

Minimizing (88) with respect to w_b and solving for $U_{o\max}$ gives the following bound on $U_{o\max}$ to ensure that $G_{den} > 0$ for all $U_o \in [0, U_{o\max}]$:

$$U_{o\max} < \begin{cases} 2\sqrt{-X_{wd}^2 + X_{wd} u_b}, & \frac{u_b}{2} < X_{wd} \leq u_b, \\ u_b, & X_{wd} < \frac{u_b}{2}. \end{cases} \tag{89}$$

Assumption 11 ensures that (89) is satisfied.

When $d_o \geq d_{safe}$, a bound $|G_{num}| < G_{nsup}$ can be found by using Assumptions 8, 11, 12, and 15:

$$\begin{aligned} G_{nsup}(w_{bsup}) &\triangleq \frac{U_{o\max} w_{bsup}(|Y_{wd}| w_{bsup} + |Z_w|)}{(X_{wd} + U_{wsup}^2)\sqrt{U_{wsup}^2 - U_{o\max}^2}} \\ &+ \frac{(U_{wsup} + U_{o\max})^2}{d_{safe} U_{wsup}} \\ &+ \omega_{o\max}\frac{U_{o\max}}{u_b} + \frac{a_{o\max}}{\sqrt{u_b^2 - U_{o\max}^2}} + \sigma_\theta. \end{aligned} \tag{90}$$

Equations (88) and (90) are even in w_b and w_{bsup}, respectively. Hence,

$$|q_{fd}(\pm w_{bsup})| < \frac{G_{nsup}(w_{bsup})}{G_{dinf}(w_{bsup})}. \tag{91}$$

Inserting (91) into (61) bounds d_{safe} and σ_θ to:

$$\frac{(U_{wsup} + U_{o\max})^2}{d_{safe} U_{wsup}} + \sigma_\theta \leq F_\theta, \tag{92}$$

where F_θ is given in (69). The design parameter κ_θ can be used to rewrite (92) as

$$\frac{(U_{wsup} + U_{o\max})^2}{d_{safe} U_{wsup}} + \sigma_\theta \leq \kappa_\theta F_\theta + (1 - \kappa_\theta) F_\theta. \tag{93}$$

Hence, conditions (70) and (71) ensure that (92) is satisfied. Condition (61) of Lemma 2 then also applies, and it follows that if $|w_b(t_0)| < w_{bsup}$, then $|w_b(t)| < w_{bsup} \; \forall \; t \geq t_0$. □

The sway velocity can be ensured to be bounded in a similar fashion by considering a pure yaw maneuver. We will do this in the next lemma, where we will use the parameter

$$F_\psi \triangleq \frac{v_{bsup}|Y_{vd}|}{|X_{vd}|} - \frac{2v_{bsup}^2|Y_{vd}| U_{o\max}}{(U_{vsup}^2 + X_{vd} u_b)\sqrt{U_{vsup}^2 - U_{o\max}^2}} - \omega_{o\max}\frac{U_{o\max}}{u_b} - \frac{a_{o\max}}{\sqrt{u_b^2 - U_{o\max}^2}}, \tag{94}$$

where $U_{vsup} \triangleq \sqrt{u_b^2 + v_{bsup}^2}$.

Lemma 4. *Consider a vehicle and an obstacle moving in the same horizontal plane. Let the vehicle kinematics be modeled by (5), the actuated surge, pitch, and yaw dynamics be modeled by (10a), (10d), and (10e), and the underactuated sway and heave dynamics be modeled by (23a)–(23b). Let the vehicle be governed by the surge controller (43a), yaw rate controller (43c), and the Flow frame yaw controller (37a). Let the control system enter collision avoidance mode at time t_1, and let the*
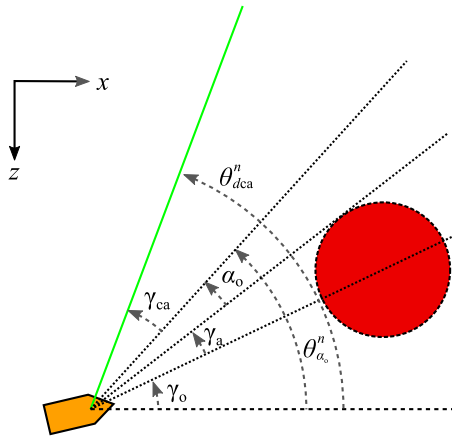
FIGURE 7 Geometry of a collision avoidance maneuver in the vertical plane. [Color figure can be viewed at wileyonlinelibrary.com]

vehicle Flow frame then be steered by the CAA algorithm in Section 5.1. Define the parameter $\kappa_\psi \in (0, 1)$, and assume that the distance between the vehicle and the obstacle satisfies $d_o(t) > d_{safe}$ $\forall$ $t \geq t_1$. If Assumptions 8–12 and 15–16 hold, the Flow frame proportional saturation σ_ψ satisfies

$$\sigma_\psi \leq \kappa_\psi F_\psi, \tag{95}$$

the safety distance d_{safe} satisfies

$$d_{safe} \geq \frac{(U_{vsup} + U_{o\,max})^2}{U_{vsup}} \frac{1}{(1 - \kappa_\psi)F_\psi}, \tag{96}$$

and the sway motion satisfies $|v_b(t_0)| < v_{bsup}$, then

$$|v_b(t)| < v_{bsup} \quad \forall\, t \geq t_0. \tag{97}$$

The proof of Lemma 4 is equivalent to the proof of Lemma 3.

6.3 | Minimum switching distance

In this section, we will use the bound on sway and heave from the previous section to derive a minimum safety distance guaranteeing that the vehicle is able to safely reach the desired heading and pitch from the collision avoidance algorithm.

Lemma 5. *Let the vehicle kinematics be modeled by* (5), *the actuated surge, pitch, and yaw dynamics be modeled by* (10a), (10d), *and* (10e), *and the underactuated sway and heave dynamics be modeled by* (23a)–(23b). *Let the vehicle be controlled by the feedback linearizing controllers* (43) *and the Flow frame controller* (34). *At a time $t_1 \geq t_0$, let the control system enter collision avoidance mode according to the switching rule in Section* 5.3, *and let the Flow frame heading and pitch then be set by the collision avoidance law* (51). *Furthermore,*
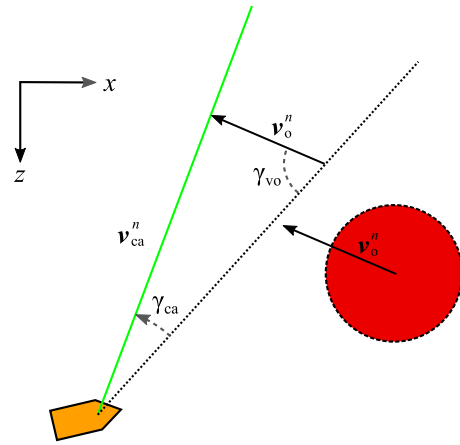
FIGURE 8 An alternative expression for γ_{ca} can be found using the sine rule on this triangle. [Color figure can be viewed at wileyonlinelibrary.com]

let Assumptions 8–16 be satisfied, the vehicle speed satisfy $U_b < U_{bsup} = \sqrt{u_{bd}^2 + v_{bsup}^2 + w_{bsup}^2}$, and the switching distance satisfy

$$d_{switch} \geq U_{o\,max} t_\epsilon + d_{safe} + d_{turn} + d_{T_b}, \tag{98}$$

where

$$t_\epsilon \triangleq \max_j \left(T_b + \left(\frac{\pi}{\sigma_j} - \frac{1}{k_j} \right) - \frac{\ln(k_j \epsilon / \sigma_j)}{k_j} \right), \quad j = \{\psi, \theta\}, \quad \epsilon \in \left(0, \frac{\pi}{2}\right] \tag{99}$$

is the maximum amount of time the Flow frame yaw controller (37a) will use to make the vehicle converge to within ϵ rad of V_c, and

$$d_{turn} \triangleq \max_j \left(\frac{U_{bsup}}{\min(\sigma_j, k_j \pi 2)} \right), \quad j = \{\psi, \theta\} \tag{100}$$

upper bounds the distance traveled by the vehicle toward the obstacle when making a complete 180° turn. The distance d_{T_b} is

$$d_{T_b} \triangleq U_{bsup} T_b. \tag{101}$$

Then, the vehicle is able to converge to within ϵ rad of V_c before the obstacle can come within the distance d_{safe}.

Proof. The main idea behind the proof is to show that the distance traveled by the obstacle during the convergence time t_ϵ is not sufficient to reduce the distance between the obstacle and the vehicle trajectory to less than d_{safe}. This is illustrated in Figure 9.

We consider a worst case scenario with an obstacle of infinite size, $R_o \to \infty$. The half apex angle of the vision cone angle is then $\gamma_a = \pi/2$. Furthermore, the vehicle and obstacle move at maximum speed, that is $U_b(t_1) = U_{bsup}$ and $U_o(t_1) = U_{o\,max}$. We assume, without loss of generality, that the obstacle is ahead of the vehicle along the x_n-axis of the NED frame, such that $x_o^n(t_1) - x_b^n(t_1) = d_{switch}$, while $y_o^n(t_1) = y_b^n(t_1)$ and $z_o^n(t_1) = z_b^n(t_1)$. Furthermore, we assume that the vehicle and

obstacle move straight toward each other at time t_1. The worst case behavior of the obstacle is then to continue moving straight ahead at maximum speed.

At time t_1, when the control system enters collision avoidance mode, the vehicle starts to make a turn toward ψ_{dca}^n and θ_{dca}^n. There will then be a jump in the desired yaw and pitch rate from the Flow frame controller, and the rate smoothing will commence. The smoothing is complete at the latest at time $t_1 + T_b$. Since $\tilde{\psi}_f^n$ and $\tilde{\theta}_f^n$ both lie in the interval $(-\pi, \pi]$, the maximum error at time $t = t_1 + T_b$ is π radians in each direction. The convergence time from $|\tilde{\psi}_f^n| = \pi$ to $|\tilde{\psi}_f^n| = \sigma_\psi/k_\psi$ is found from (37a) to be $\pi/\sigma_\psi - 1/k_\psi$, which is ensured to be positive by Assumption 13. From this point, the course converges exponentially, and hence the convergence time from $|\tilde{\psi}_f^n| = \sigma_\psi/k_\psi$ to $|\tilde{\psi}_f^n| < \epsilon$ is $\frac{\ln(k_\psi \epsilon / \sigma_\psi)}{k_\psi}$. Similar convergence times can be found for $|\tilde{\theta}_f^n|$.

It follows that the total time from t_1 until the vehicle's velocity vector is less than $\sqrt{2}\epsilon$ away from V_c is upper bounded by t_ϵ as defined in (99). During this time, the obstacle will, at worst, have traversed $U_{o\,max} t_\epsilon$ toward the vehicle.

During the smoothing interval $t \in (t_1, t_1 + T_b]$, the distance covered by the vehicle toward the obstacle is upper bounded by d_{T_b}. In a worst case scenario, the vehicle then has to turn completely around. Assumption 13 ensures that the vehicle will move at most d_{turn} towards the obstacle when turning.

Hence, if condition (98) holds, then the distance between the obstacle and the vehicle trajectory will not be reduced to less than d_{safe} before the vehicle velocity direction has converged to within ϵ rad of V_c. It follows that the obstacle is thus more than d_{safe} meters from the vehicle, which concludes the proof. $\square$

Remark 10. In the proof of Lemma 1, we have used an obstacle of infinite size. In practice, a vehicle approaching a very large obstacle may not be able to sense the edges of the obstacle due to sensor range limitations. In such a case, the obstacle will appear smaller to the vehicle while it moves toward one of the edges of the vision cone created by the part of the obstacle within sensor range. The vehicle will then keep moving along the edge of this vision cone, until the obstacle has been avoided.

6.4 | Safe target reaching

We have now proved that a vehicle following the collision avoidance law (51) is sure to keep a minimum distance away from the obstacle (Lemma 1), that the vehicle sway and heave will remain bounded during a maneuver around a moving obstacle (Lemma 2–4), and we have found a minimum distance at which the vehicle must enter collision avoidance mode to ensure that it is able to turn away in time (Lemma 5). In this section, we will use these Lemmas to prove that the vehicle will safely traverse an environment containing an obstacle and reach the target position. This is the main theorem of the paper. Before we state the theorem, we make the assumptions that the vehicle is able to start safely, and that the obstacle does not cover the target.

Assumption 17.

$$\theta_f^n(t_0) \in [\theta_{fmin}, \theta_{fmax}]. \tag{102}$$

Assumption 18.

$$d_o(t_0) > d_{switch}. \tag{103}$$

Assumption 19. The distance d_{ot} from the obstacle to the target position p_t^n satisfies

$$d_{ot} > \frac{R_o}{\cos(\alpha_o)} - R_o \quad \forall\, t \geq t_0. \tag{104}$$

Remark 11. Vehicle safety is guaranteed even if this assumption is not met, but it is then not ensured that the target will be reached.

Due to the smoothing time T_b of the yaw rate reference signal, we also need at least one of the following assumptions to hold:

Assumption 20. The obstacle will not actively turn toward the vehicle when $d_o \leq d_{switch}$.

or

Assumption 21. The smoothing time T_b is small enough to be neglected, that is

$$(U_{o\,max} + U_{bsup})T_b \ll d_{safe}. \tag{105}$$

Remark 12. These assumptions require the obstacle to at least not be actively seeking a collision with the vehicle if the vehicle dynamics make T_b large. Specifically, if the vehicle lacks maneuverability, the safety distance d_{safe} must either be chosen large enough to account for the limited turning capabilties, or the vehicle must rely on at least some level of cooperation from the obstacle. As 2D examples, we could consider an oil tanker which use a very long time to initiate a turn, and thus would rely an Assumption 20, or we could consider a small speed boat, where Assumption 21 can safely be made.

Theorem 1. *Let Assumptions 8–19 and either 20 or 21 hold, the avoidance angle α_o satisfy*

$$\alpha_o \in \left[\cos^{-1}\left(\frac{R_o}{R_o + d_{safe}}\right) + \sqrt{2}\epsilon, \frac{\pi}{2}\right), \tag{106}$$

where

$$\epsilon \in \left(0, \frac{\pi}{2\sqrt{2}} - \frac{R_o}{\sqrt{2}(R_o + d_{safe})}\right), \tag{107}$$

and the switching distance satisfy

$$d_{switch} \geq U_{o\,max} t_\epsilon + d_{safe} + d_{turn} + d_{T_b}. \tag{108}$$

Moreover, let the safety distance satisfy $d_{\mathrm{safe}} \geq \max\{d_{\mathrm{safe}\psi}, d_{\mathrm{safe}\theta}\}$, *where*

$$d_{\mathrm{safe}\psi} \geq \frac{(U_{v\mathrm{sup}} + U_{o\max})^2}{U_{v\mathrm{sup}}} \frac{1}{(1 - \kappa_\psi)F_\psi}, \tag{109}$$

and

$$d_{\mathrm{safe}\theta} \geq \frac{(U_{w\mathrm{sup}} + U_{o\max})^2}{U_{w\mathrm{sup}}} \frac{1}{(1 - \kappa_\theta)F_\theta}. \tag{110}$$

Assume that the saturations in the Flow frame yaw and pitch controllers satisfy

$$\sigma_\psi \leq \kappa_\psi F_\psi, \tag{111}$$

$$\sigma_\theta \leq \kappa_\theta F_\theta, \tag{112}$$

and that the initial sway and heave speeds satisfy

$$v_b(t_0) < v_{b\mathrm{sup}}, \tag{113}$$

$$w_b(t_0) < w_{b\mathrm{sup}}, \tag{114}$$

where $v_{b\mathrm{sup}} > 0$ *and* $w_{b\mathrm{sup}} > |Z_w|/|Y_{wd}|$.

Furthermore, let the vehicle kinematics be modeled by (5), *the actuated surge, pitch, and yaw dynamics be modeled by* (10a), (10d), *and* (10e), *and the underactuated sway and heave dynamics be modeled by* (23a)–(23b). *Finally, let the vehicle be governed by the surge, yaw, and pitch rate controllers* (43), *the Flow frame controllers* (37), *the guidance laws* (31) *and* (32), *and the CA law* (51). *Then, there exists a time* $t_f \geq t_0$ *such that*

$$\|\boldsymbol{p}_t^{nb}(t_f)\| \leq d_a, \tag{115}$$

while it is ensured that

$$d_o(t) \geq d_{\mathrm{safe}} \quad \forall\, t \in [t_0, t_f], \tag{116}$$

and

$$\theta_f^n(t) \in [\theta_{f\min}, \theta_{f\max}] \quad \forall\, t \in [t_0, t_f]. \tag{117}$$

Hence, the control objectives (28), (29), *and* (30) *are met.*

Proof. Conditions (109)–(114), Lemma 3 and Lemma 4 ensure that $U_b < U_{b\mathrm{sup}} \,\forall\, t \in [t_0, t_f]$. Consider a time $t_1 \geq t_0$, at which the vehicle enters collision avoidance mode in accordance with (56). The vehicle then chooses a direction which minimizes the cost function C, and starts turning toward this direction.

Lemma 5 ensures that there is a time $t_2 \geq t_1 + T_b$ when the angular distance between the vehicle's velocity direction and the closest point on the compensated vision cone will be less than ε radians, while $d_o(t) > d_{\mathrm{safe}}$ for $t \in [t_1, t_2]$. Since the yaw rate reference signal r_{bd} and
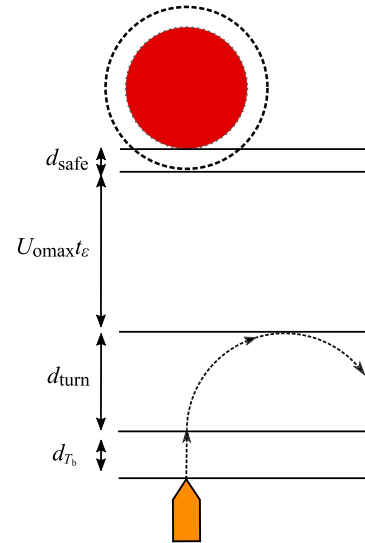
FIGURE 9 Illustration of the minimum required switching distance. [Color figure can be viewed at wileyonlinelibrary.com]

the pitch rate reference signal q_{fd} are smooth, the error dynamics of the Flow frame controllers (34) have a locally exponentially stable equilibrium at the origin. Hence, it is ensured that the angular distance between $\dot{\boldsymbol{p}}_b^n$ and V_c remains less than ε radians until a time $t_3 \geq t_2$, at which time the vehicle exits collision avoidance mode.

In a coordinate frame moving with the obstacle's velocity vector $\boldsymbol{v}_{o/n}^n$, the direction of the vehicle's velocity vector is less than $\sqrt{2}\varepsilon$ radians from the extended vision cone $\mathscr{V}_e$. Hence, condition (106) and Lemma 1 then ensure that $d_o(t) \geq d_{\mathrm{safe}} \quad \forall\, t \in [t_2, t_3]$.

The guidance laws in (31) and (32) steer the vehicle toward the target. Hence, it is ensured that there exists a finite time t_f when $\|\boldsymbol{p}_t^{nb}(t_f)\| \leq d_a$, fulfilling condition (115).

While the definition of C ensures that $\theta_{\mathrm{dca}}^n \in [\theta_{f\min}, \theta_{f\max}]$, the definition of the pitch guidance law (32) ensures that $\theta_{\mathrm{dg}}^n \in [\theta_{f\min}, \theta_{f\max}]$. Assumption 17 and the pitch control law (37b) then ensure that condition (117) is fulfilled. □

Theorem 1 provides conditions under which collision avoidance is guaranteed. Specifically, we have provided a minimum switching distance d_{switch}, a minimum safety distance d_{safe} and lower bounds on the Flow frame controller saturations σ_θ and σ_ψ. In the next section, we will verify this analysis through simulations, before we present the experimental results in Section 8.

7 | SIMULATIONS

This section contains simulations of different collision avoidance scenarios to illustrate the behavior of the algorithm, and to verify the theoretical results in Theorem 1. The simulation parameters are summarized in Table 2.

The simulated vehicle is a Hugin AUV (Hagen et al., 2003) of approximately the same kind as the one used for the experiments in

TABLE 2 Simulation parameters

u_b	2.0 m/s	θ_{fmin}	−0.5 rad
v_{bsup}	2.0 m/s	θ_{fmax}	0.5 rad
w_{bsup}	2.0 m/s	$p_b^n(t_0)$	$[0, 0, 0]^T$ (m)
R_o	20 m	U_o	1.0 m/s
ω_{omax}	0 rad/s	a_{omax}	0 m/s^2
d_{safe}	11 m	σ_θ	0.15 rad/s
α_o	0.94 rad	σ_ψ	0.15 rad/s
d_{switch}	61 m	$p_t^n(t_0)$	$[150, 0, 0]^T$ (m)
ϵ	0.05 rad	T_b	1.0 s
λ	50		

Section 8. The hydrodynamic parameters of the AUV make $F_\theta = 0.64$ and $F_\psi = 0.70$. Hence, the values chosen for σ_ψ, σ_θ, and d_{safe} satisfy the conditions of Theorem 1 with $\kappa_\theta = \kappa_\psi = 0.25$. Furthermore, it can be verified the obstacle speed satisfies (27). The avoidance angle α_o and the switching distance d_{switch} are set using Equations (106) and (108), respectively.

The first scenario contains a head on situation and is shown in Figure 10. The initial position of the obstacle is $p_o^n(t_0) = [100, 5, 5]^T$ m, and it moves along a straight line with $\psi_o^n = \pi$ rad and $\theta_o^n = 0$ rad.

When the vehicle enters collision avoidance mode, the obstacle is slightly below and to the starboard side of it. The vehicle thus makes a port turn and pitches upward, choosing a safe direction which minimizes the cost function C (55). The vehicle continues the maneuver until the line of sight to the target becomes safe, at which point it exits collision avoidance mode according to the switching criterium in Section 5.3, and proceeds toward the target.

The sway and heave speeds of the vehicle are shown in Figure 11. They are both well within the limit of 2 m/s, which verifies Lemma 3 and 4. The magnitude of the difference between the Flow frame rates q_f and r_f obtained from using the analysis model (22a)–(22b) and the more precise model in (19) is shown in the lower part of the figure. The error remains small throughout the maneuver, which justifies the use of the analysis model when deriving the bounds on the Flow frame controller saturation parameters σ_θ and σ_ψ, and the safety distance d_{safe}.

The distance between the vehicle and the obstacle remains above the safety distance d_{safe} throughout the maneuver, which can be seen in Figure 12. Furthermore, the Flow frame pitch angle θ_f^n remains within $[\theta_{fmin}, \theta_{fmax}]$. Thus, the simulation shows that the vehicle is able to start the collision avoidance maneuver early enough to safely reach the desired velocity direction during collision avoidance, and that it maneuvers around the obstacle without exceeding the bounds on v_b, w_b, and θ_f^n. Hence, the simulation verifies the results of Theorem 1.
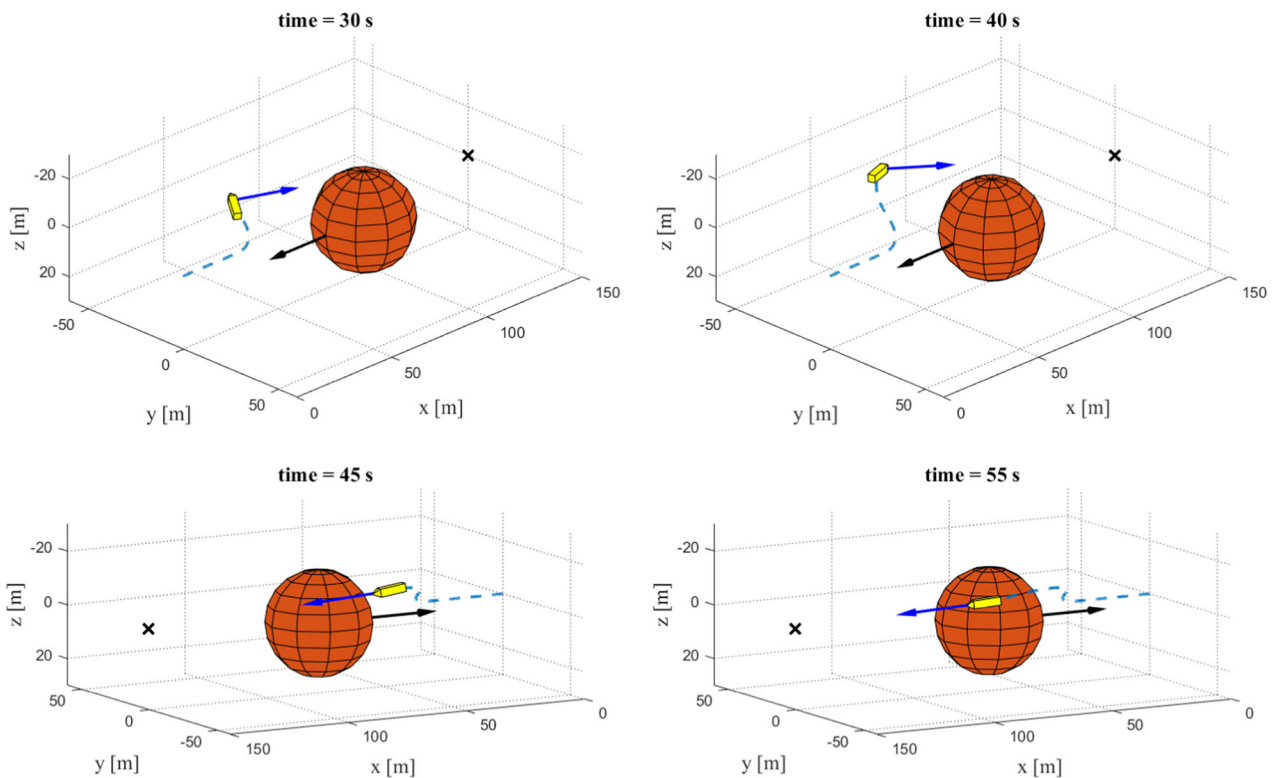

FIGURE 10 A scenario where the vehicle and obstacle meet head on head. The vehicle is the yellow polyhedron, and the obstacle is the red sphere. The blue line is the vehicle trajectory, the target is marked by an "X," and the direction obstacle velocity is shown as a black arrow. The blue arrow shows the nominal desired velocity direction of the vehicle, that is, the desired direction of the vehicle if it were not in collision avoidance mode. The vehicle size is exaggerated for clarity, and the view has been rotated in the lower two snapshots of the simulation. [Color figure can be viewed at wileyonlinelibrary.com]
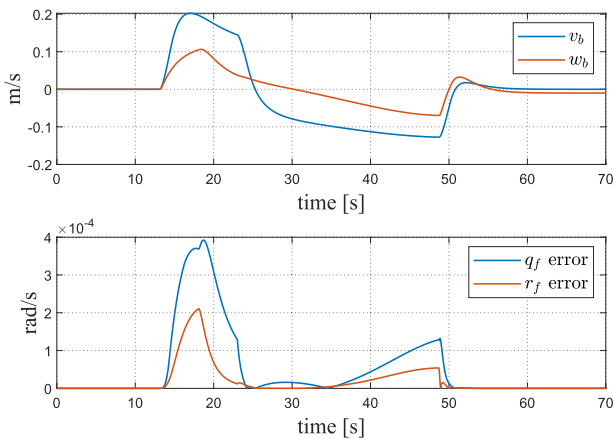
FIGURE 11 The sway v_b and heave w_b speeds of the vehicle during the first scenario (top), and the error resulting from using the analysis model to find q_f and r_f (bottom). [Color figure can be viewed at wileyonlinelibrary.com]
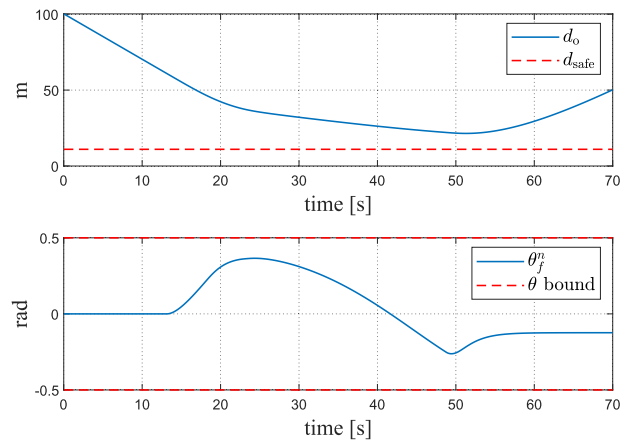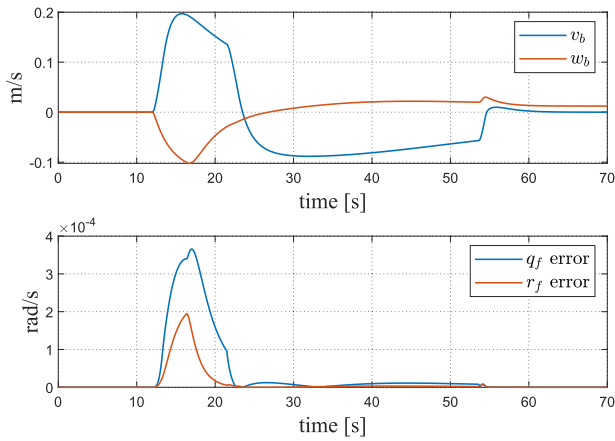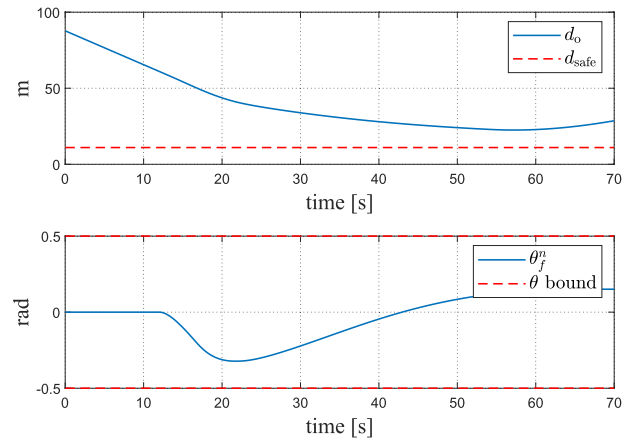
FIGURE 12 The distance d_o between the vehicle and the obstacle during the first scenario (top) and the Flow frame pitch angle θ_f^n (bottom). [Color figure can be viewed at wileyonlinelibrary.com]

In the next scenario, displayed in Figure 13, the obstacle crosses in front of the vehicle, moving horizontally. Upon entering collision avoidance, the vehicle thus chooses a ray of V_c which takes it behind the obstacle, in accordance with (55). Since the vehicle and obstacle both move horizontally when collision

avoidance is initialized, the choice of going above or below the obstacle becomes random. In this case, the vehicle maneuvers below the obstacle.

As shown in Figures 14 and 15, the limits on sway, heave, and Flow frame pitch are upheld throughout the maneuver, and the distance to the obstacle is never less then d_{safe}. Thus, this scenario also verifies the results of Theorem 1.
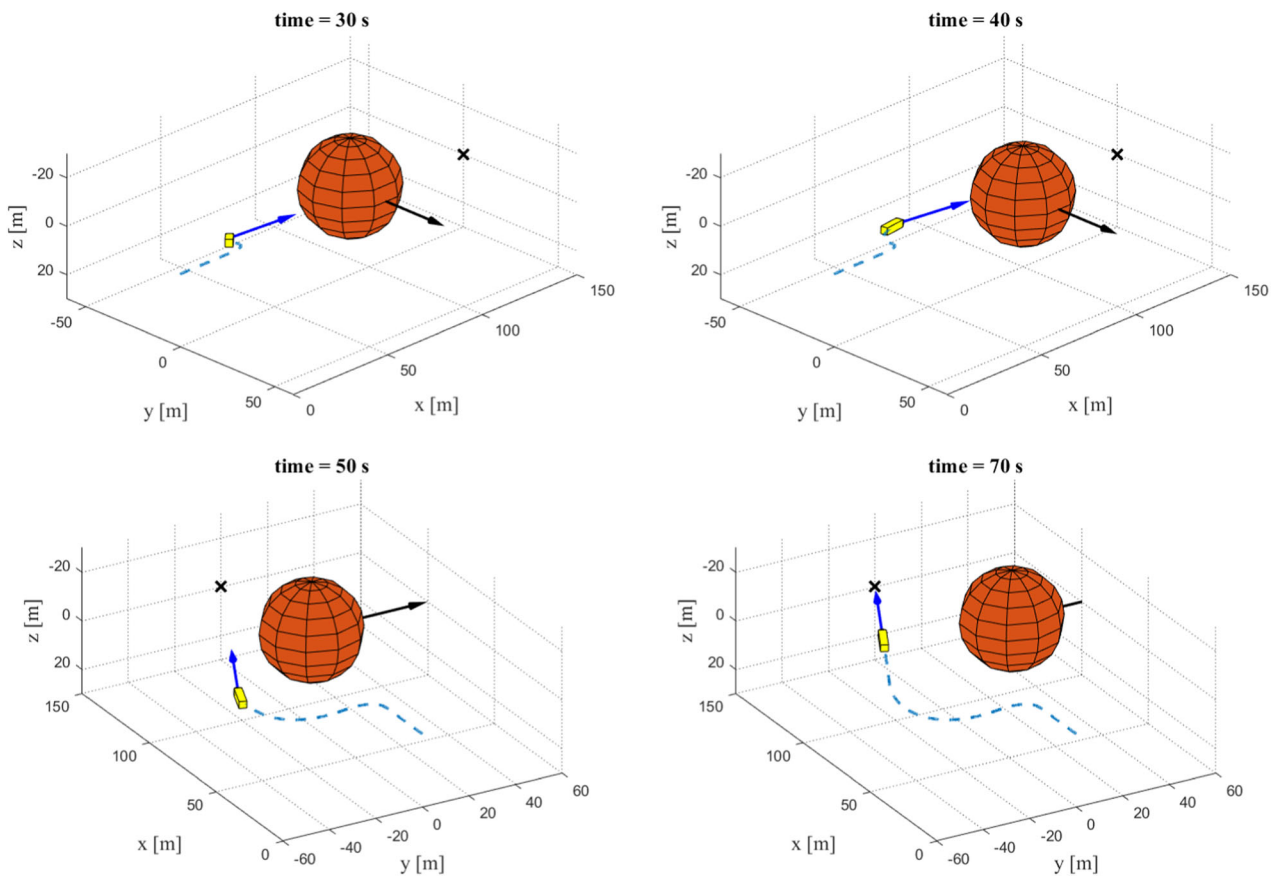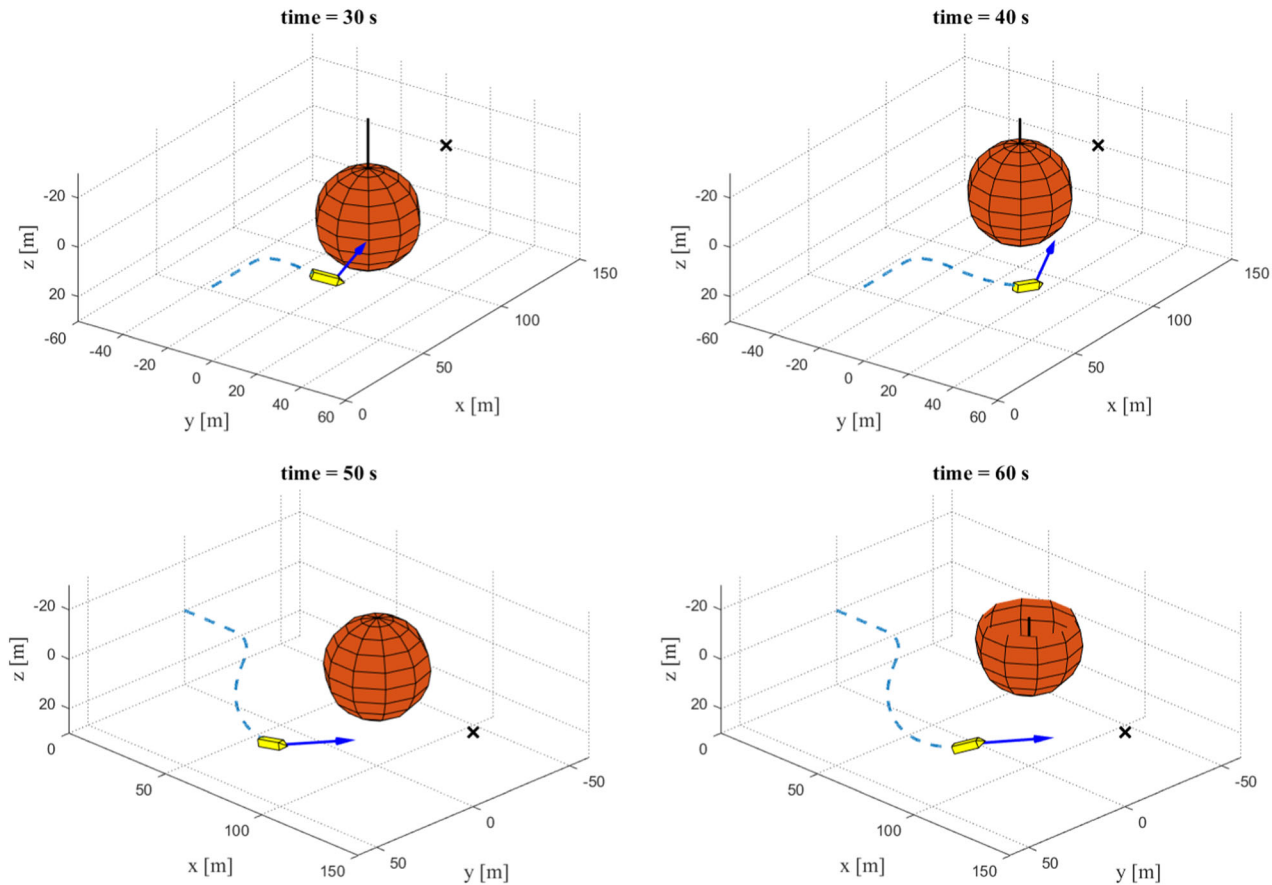

FIGURE 13 A scenario where the obstacle crosses horizontally in front of the vehicle. [Color figure can be viewed at wileyonlinelibrary.com]
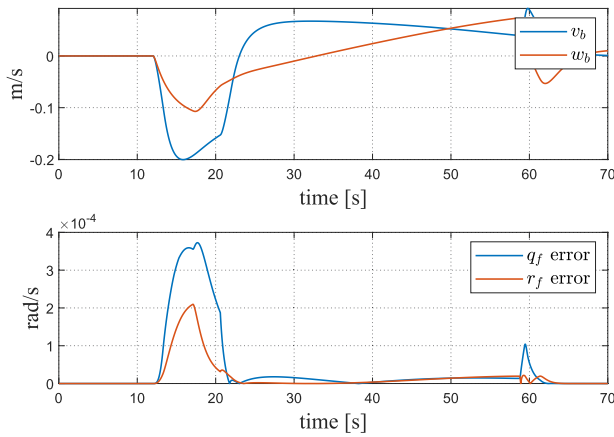
FIGURE 14 The sway v_b and heave w_b speeds of the vehicle during the second scenario (top) and the error resulting from using the analysis model to find q_f and r_f (bottom). [Color figure can be viewed at wileyonlinelibrary.com]
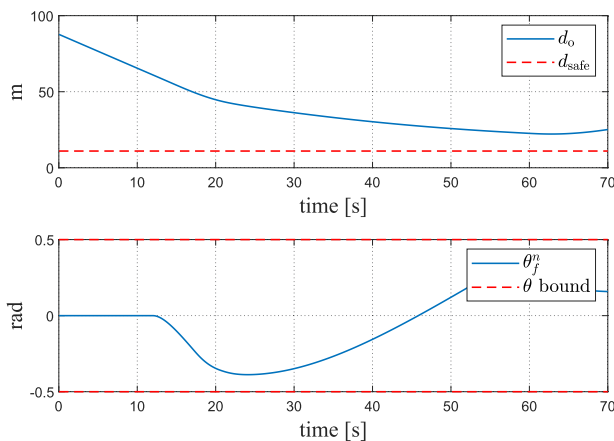
FIGURE 15 The distance d_o between the vehicle and the obstacle during the second scenario (top) and the Flow frame pitch angle θ_f^n (bottom). [Color figure can be viewed at wileyonlinelibrary.com]

Figures 16, 17, and 18 shows the final scenario, where the obstacle crosses in front of the vehicle from below, moving vertically. The vehicle maneuvers below the obstacle while keeping it on the port side, until the direction toward the target becomes safe. The vehicle then exits collision avoidance mode and proceeds with nominal guidance. As in the previous scenarios, the bounds on the vehicle sway and heave, and on the Flow frame pitch are upheld, and the vehicle remains at a safe distance to the obstacle throughout the maneuver.

FIGURE 16 A scenario where the obstacle crosses vertically in front of the vehicle. [Color figure can be viewed at wileyonlinelibrary.com]

FIGURE 17 The sway v_b and heave w_b speeds of the vehicle during the third scenario (top) and the error resulting from using the analysis model to find q_f and r_f (bottom). [Color figure can be viewed at wileyonlinelibrary.com]

7.1 | Monte Carlo simulations

To further validate the theoretical results of Section 6, we have performed a series of simulations with probabilistic obstacle parameters, which are drawn from several uniform distributions as follows: The obstacle radius is in the interval (10, 100) m. The distance from the vehicle to the obstacle center is 200 m, which ensures that the vehicle always starts further away from the obstacle than d_{switch}. The direction from the vehicle to the obstacle center is in the interval $(-\pi/2, \pi/2)$ in the horizontal and vertical direction, placing the obstacles on a quarter sphere in between the vehicle and the target. The obstacle speed is drawn from the interval (0.5, 1.5) m/s. The obstacle heading was drawn from $(0, \pi)$ if $y_o^n(t_0) < = 0$, and $(-\pi, 0)$ if $y_o^n(t_0) > 0$. Thus, the obstacle tended to move toward rather than away from the y^n-axis, increasing the probability of creating a collision avoidance maneuver. Similarly, the obstacle pitch was drawn

TABLE 3 Results from the Monte Carlo simulations

	Max	Min	Mean	Std. dev
$t_f - t_0$ (s)	1,078.3	995.2	1,000.4	8.8
$d_{\min}$ (m)	60.8	16.6	30.8	9.2
$\max(|\theta_f^n|)$ (rad)	0.46	0.0	0.21	0.12
$\max(|v_b|)$ (m/s)	0.24	0.01	0.12	0.07
$\max(|w_b|)$ (m/s)	0.12	0.00	0.07	0.03

from $(0, \pi/4)$ if $z_o^n(t_0) < = 0$, and $(-\pi/4, 0)$ if $z_o^n(t_0) > 0$. The switching distance d_{switch} and avoidance angle α_o are in each run set using Equations (108) and (106), respectively. The remainder of the parameters are as described in Table 2.

A total of 5,000 simulations have been executed. Of these, 1,873 runs contain collision avoidance maneuvers. For each run, the completion time, the minimum distance to the obstacle, the maximum magnitude of the flow frame pitch angle and the maximum vehicle sway and heave velocities where recorded. Table 3 summarizes these results, showing the maximum, minimum, mean, and standard deviation of these variables across the runs containing collision avoidance maneuvers.

Figure 19 shows the distribution of the completion times, the minimum distances and the maximum Flow frame pitch magnitude of the runs containing collision avoidance maneuvers. Both Table 3 and Figure 19 show that the vehicle reached the target in all cases, while staying at least $d_{\text{safe}} = 11\,\text{m}$ away from the obstacle. Furthermore, the bounds on the Flow frame pitch angle is within the maximum limit of ± 0.5 rad, and the vehicle sway and heave are well within their limits, indicating that these bounds are conservative.

While a complete robustness analysis is beyond the scope of this paper, it is still of interest to examine the performance of the collision avoidance algorithm in the presence of model uncertainties. This is particularly so since the Flow frame controller and the low-level controllers employed in this paper to steer the vehicle toward the
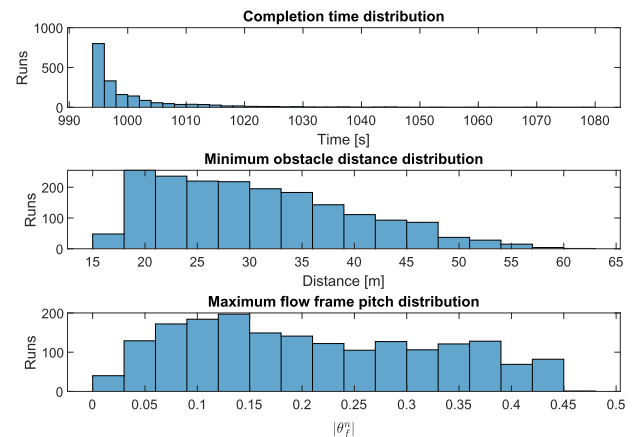

FIGURE 18 The distance d_o between the vehicle and the obstacle during the third scenario (top) and the Flow frame pitch angle θ_f^n (bottom). [Color figure can be viewed at wileyonlinelibrary.com]

FIGURE 19 Distribution of the completion time, minimum distance to the obstacle and maximum value of the Flow frame pitch angle during the Monte Carlo simulations. [Color figure can be viewed at wileyonlinelibrary.com]

TABLE 4 Results from the Monte Carlo simulations with perturbed control model parameters

	Max	Min	Mean	Std. dev
$t_f - t_0$ (s)	1,112	993	1,013	20.4
d_{min} (m)	60.5	15.1	26.5	9.6
$\max(|\theta_f^n|)$ (rad)	0.47	0.03	0.37	0.08
$\max(|v_b|)$ (m/s)	0.48	0.02	0.21	0.08
$\max(|w_b|)$ (m/s)	0.11	0.02	0.10	0.01

FIGURE 20 Distribution of the completion time, minimum distance to the obstacle, and maximum value of the Flow frame pitch angle during the Monte Carlo simulations containing perturbation on the vehicles control model. [Color figure can be viewed at wileyonlinelibrary.com]

directions given by the algorithm rely heavily on model parameters, which in many cases can be uncertain. To examine this, we have repeated the above series of simulations. In this case, however, the mass matrix M of the vehicle model (6) used in the vehicle controllers is multiplied by a factor drawn uniformly from (0.8, 1.2). As shown in (8), by perturbing M we also perturb the Coriolis matrix C. Similarly, the damping matrix D is also multiplied by a factor drawn from (0.8, 1.2). Note that the vehicle model used to simulate the vehicle dynamics is kept constant, only the model used by the controllers are perturbed. The perturbation is kept constant for each run, and the obstacle parameters of the simulations are the same as the parameters in the set described above.

The results of the Monte Carlo simulations with perturbed control model parameters are shown in Table 4 and Figure 20. As in the simulations with an accurate control model, the vehicle manages to stay outside of the safety distance for all runs, and the Flow frame pitch angle and the sway and heave speeds remain within their limits. The reduced control accuracy of the vehicle does, however, make it come closer to the obstacle than in the nominal case. This implies that if the system has uncertain dynamic parameters, it may be necessary make the avoidance angle α_o and switching distance d_{switch} larger than the theoretical minimums given by (106) and (108). Additionally, the maneuvers both take a longer time on average, and the increased sway and heave speeds indicate that a larger control effort was employed during the maneuver.

7.2 | Multiple obstacles

In this section, we present simulations demonstrating the applicability of the constant avoidance angle algorithm to multiobstacle scenarios. For these simulations, the radius of the obstacle is reduced to 10 m, while the avoidance angle α_o is increased to 1.15 rad. Otherwise, the simulation parameters are the same as for the single-obstacle simulations in the previous section.

The first scenario contains a cluster of five obstacles approaching the vehicle head on. Snapshots from the simulation are shown in Figure 21, where it can be seen that the vehicle heads up and to starboard around the obstacles. The vehicle successfully maneuvers around the cluster as if it was a single, nonconvex obstacle. When the line of sight to the target comes outside of the vision cones of all the
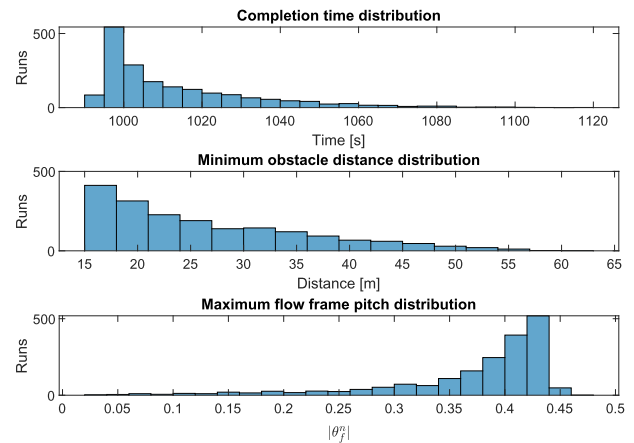
obstacles, the vehicle exits collision avoidance mode and proceeds toward it. At no point in the maneuver is the vehicle closer than d_{safe} to any of the obstacles, as seen in Figure 22.

In the second scenario, illustrated in Figure 23, the vehicle first encounters two obstacles crossing in front of it. While the vehicle maneuvers to avoid these obstacles, it encounters a third obstacle, and adjusts its course and pitch to avoid this obstacle as well. After the last obstacle has been safely avoided, the vehicle proceeds towards the target. Again, as seen in Figure 24, the distance to each of the obstacles were always above the safety distance.

8 | EXPERIMENTS

The constant avoidance angle algorithm described in Section 5, as well as the pure pursuit guidance law in Section 4.1, have been implemented in an experimental setup on the Hugin HUS AUV, shown in Figure 25. This vehicle is owned and operated by the Norwegian Defense Research Establishment (FFI) and can be operated from any appropriate vessel of opportunity. For this experiment, the AUV was operated from the FFI research vessel H.U. Sverdrup II. The algorithms were implemented using a back seat driver interface enabling third party and prototype software modules to take control of the vehicle.

The exact hydrodynamic model of the vehicle is not available, but it is similar to the vehicle simulated in the previous section. Furthermore, the implementation details of the low-level controllers are not available; however, the modular nature of the collision avoidance algorithm and guidance law made it possible to send desired pitch and heading to the controllers. To convert the pitch and heading angles from the collision avoidance algorithm and from the target
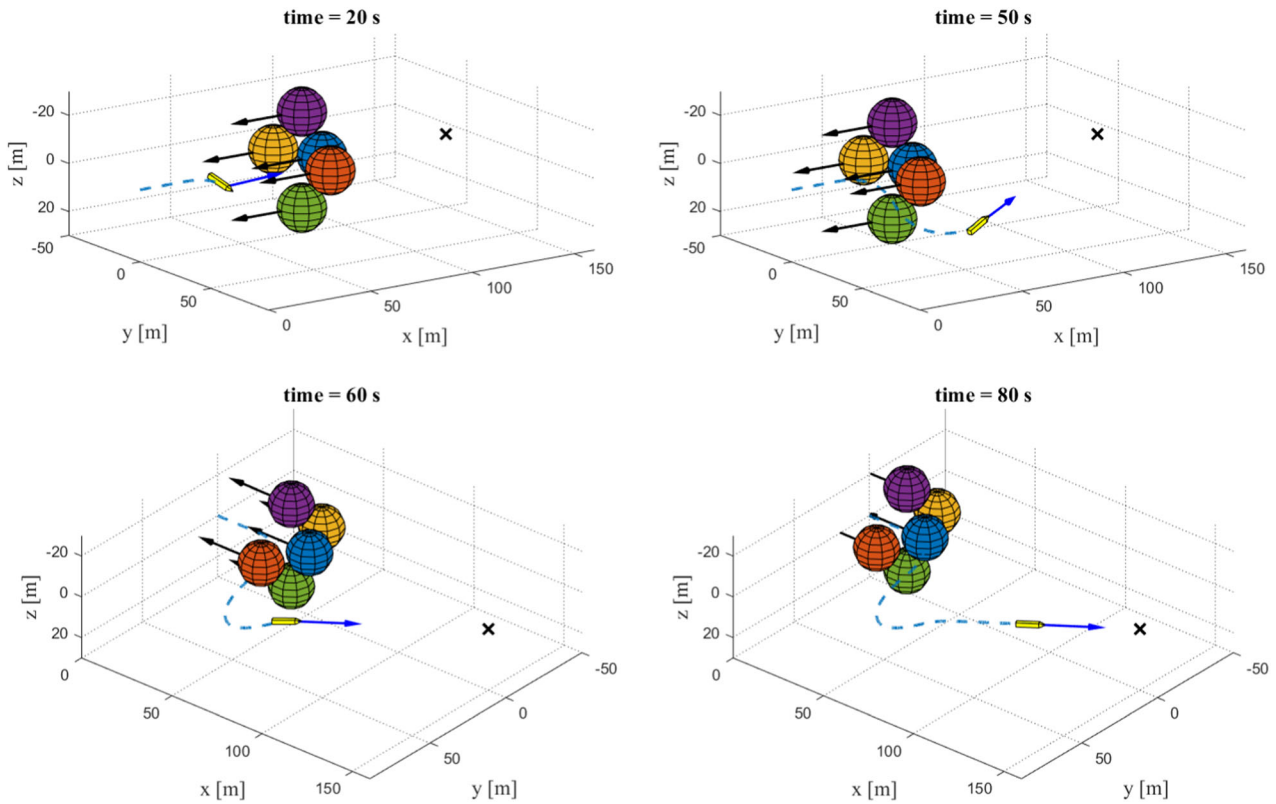
FIGURE 21 Snapshots from a simulation where the vehicle meets a cluster of five obstacles. [Color figure can be viewed at wileyonlinelibrary.com]

reaching guidance law from the Flow frame to the Body frame, Equations (15) and (16) has to be inverted. This is not straight forward, and the following small angle approximation were used for the experiment:

$$\theta_{bd}^n \approx \theta_{fd}^n - \alpha_b, \tag{118}$$
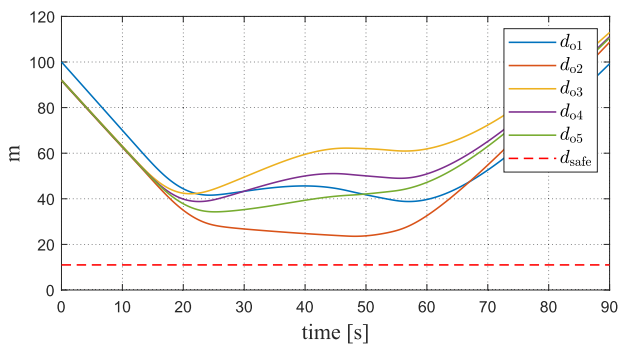
$$\psi_{bd}^n \approx \psi_{fd}^n - \beta_b, \tag{119}$$

FIGURE 22 The distances to each of the obstacles in the first multiobstacle scenario. [Color figure can be viewed at wileyonlinelibrary.com]

where θ_{bd}^n and ψ_{fd}^n are the desired pitch and yaw of the Body frame, respectively. Note that this approximation is not required for vehicles equipped with a velocity controller. The vehicle's propeller speed is set to a constant value to give a surge velocity of about 2 m/s.

The vehicle's global navigation state, containing the position and attitude of the vehicle as well as their velocities and accelerations, were provided by a high-end aided inertial navigation system (Jalving, Gade, Hagen, & Vestgard, 2004). During the runs, the navigation system was aided by velocity measurements from a Doppler velocity log, by depth measurements and by occasional acoustic position updates from the mother vessel.

For the experiments, the cost function used to choose a safe ray was modified to choose the ray minimizing the maximum heading or pitch error:

$$C_{\exp} \triangleq \begin{cases} |\boldsymbol{e}_\rho|_\infty, & \theta_\rho^n \in [\theta_{f\min}, \theta_{f\max}], \\ |\boldsymbol{e}_\rho|_\infty + 2\pi, & \theta_\rho^n \notin [\theta_{f\min}, \theta_{f\max}]. \end{cases} \tag{120}$$

This cost function will tend to make the vehicle employ both the sternplanes and the rudders to avoid the obstacle.

A total of 16 runs were executed. In each of the runs, the vehicle moved towards a target position and encountered a moving obstacle along the way. To focus on the performance of the algorithm under ideal
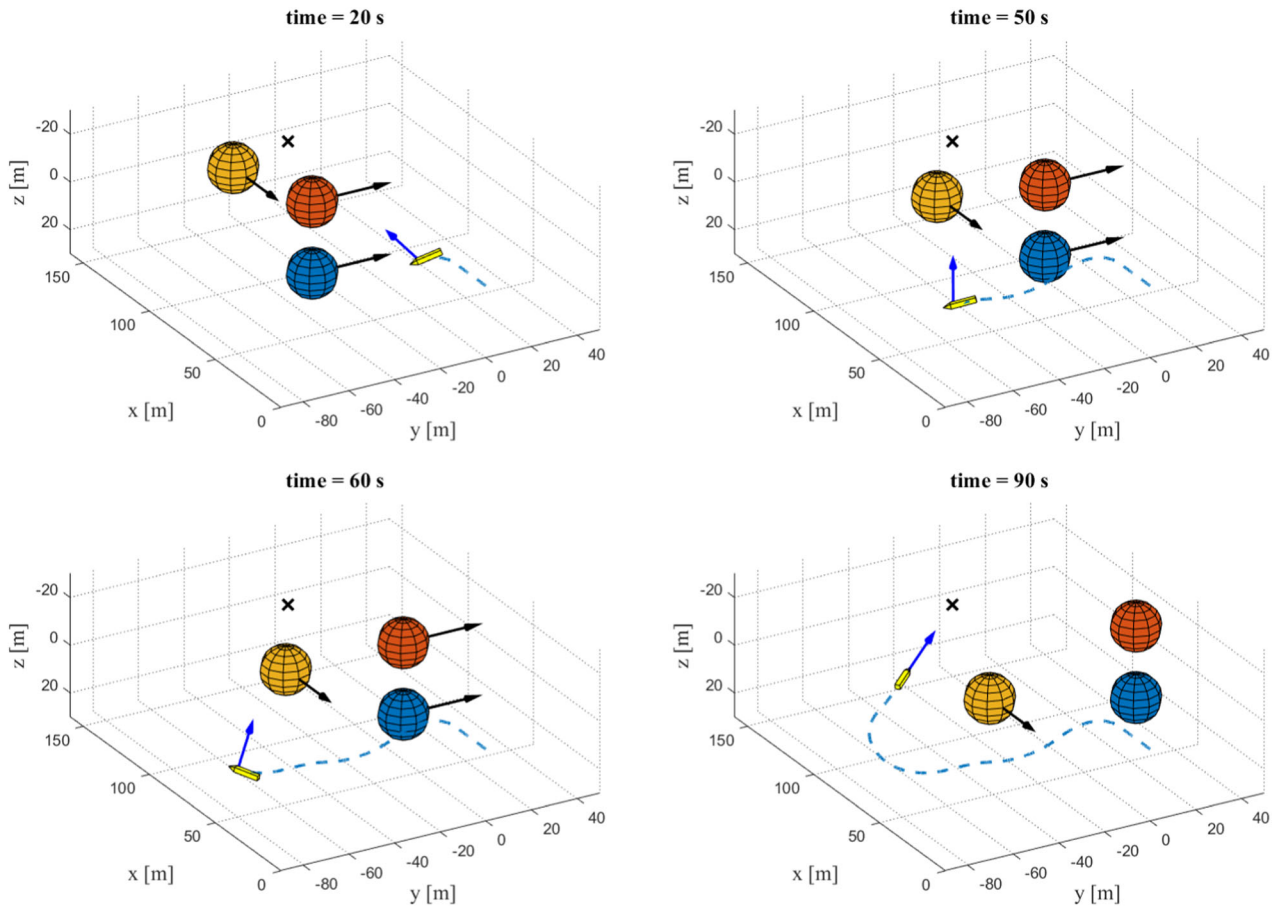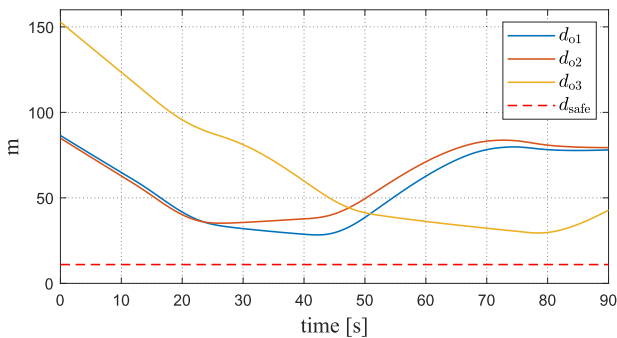
FIGURE 23 Snapshots from a simulation where the vehicle meets three obstacles, two crossing in front of it and one moving toward it. [Color figure can be viewed at wileyonlinelibrary.com]

sensing conditions, and to be able to perform more controlled underwater experiments, the vehicle encountered only virtual obstacles during the experiments. When the obstacle got too close to the vehicle, the control system entered collision avoidance mode and safely executed an avoidance maneuver before proceeding towards the target. When the target was reached, the run ended and the next run automatically began. The parameters of the experiments are shown in Table 5.

Rather than following a constant surge speed, the vehicle was set to maintain a constant thrust in the experiments. Thus, the surge speed varied during the maneuver, as it encountered damping while turning. The surge speed u_b and the total vehicle speed U_b during run 4 are shown in Figure 26. Since the constant avoidance angle algorithm proposed in this paper uses the vehicle speed as an input, the desired Flow frame heading and pitch during the maneuver readily compensated for the damping in U_b.

FIGURE 24 The distances to each of the obstacles in the second multiobstacle scenario. [Color figure can be viewed at wileyonlinelibrary.com]

FIGURE 25 The Hugin HUS vehicle. [Color figure can be viewed at wileyonlinelibrary.com]

TABLE 5 Experiment parameters

α_o	0.8 rad	u_b	~2 m/s
d_{safe}	4.4 m	U_o (Run 1–8)	1.0 m/s
d_{switch}	50 m	U_o (Run 9–16)	1.5 m/s
θ_{fmin}	−0.35 rad	R_o	10 m
θ_{fmax}	0.44 rad		

A summary of each run is shown in Table 6. The vehicle never got closer than d_{safe} from the obstacle during any of the maneuvers. However, due to an unmodeled disturbance on the vehicle and a time delay in the backseat driver system, the Flow frame pitch slightly exceeded the minimum limit on run 1, 5, 9, 12, and 15.

Figure 27 shows the maneuver of run 6, which was a head on scenario. When the vehicle got closer than 50 m to the obstacle, it entered into collision avoidance mode and began the avoidance maneuver. The obstacle was on the lower, port side of the vehicle, and hence it maneuvered up and starboard in accordance with (120). When the obstacle was safely avoided, the vehicle proceeded toward the target position. As shown in Figure 28, the distance to the obstacle remained well above the safety distance, and the Flow frame pitch remained within its limits. The sideslip β_b and angle of attack α_b remained small during the maneuver, as seen in Figure 29, justifying the small angle assumption used in the analysis.

Another example is shown in Figure 30, which displays the crossing scenario in run 4. Again, when the obstacle got closer than 50 m, the vehicle entered into collision avoidance mode. The relative
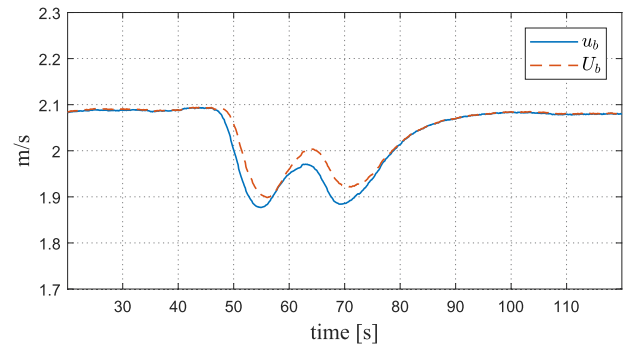
FIGURE 26 The surge speed u_b and the total vehicle speed U_b during run 4. [Color figure can be viewed at wileyonlinelibrary.com]

positions of the vehicle and the obstacle made the algorithm choose to move up and to port in accordance with (120). This makes the vehicle maneuver behind the obstacle, which is the same behavior that would result from using the optimization criterion (55). The obstacle distance remained well above the safety distance, as shown in Figure 31, and the Flow frame pitch angle stayed within its limits. Moreover, the sideslip and angle of attack, displayed in Figure 32, remained small.

9 | CONCLUSIONS AND FUTURE WORK

The constant avoidance angle algorithm proposed in this paper is a reactive algorithm for avoiding moving obstacles in three dimensions. The algorithm works by steering the vehicle so that it maintains an

TABLE 6 Experiments summary

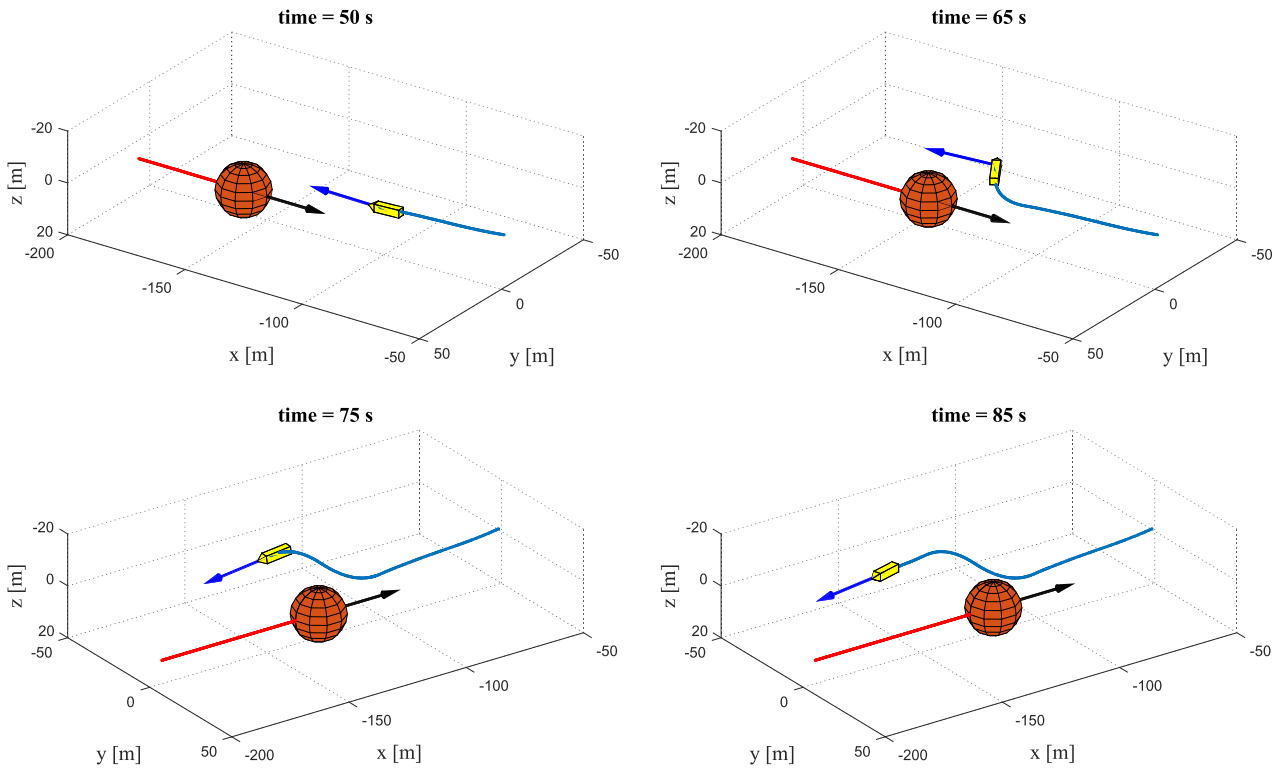| Run	Type	$min(d_o)$ (m)	$min(\theta_f^n)$ (rad)	$max\ \theta_f^n$ (rad)	$max(|v_b|)$ (m/s)	$max(|w_b|)$ (m/s)	z_o^n (m)
1	Head on	24.5	−0.37	0.13	0.49	0.36	0.0
2	Head on	20.0	−0.33	0.35	0.48	0.32	10.0
3	Crossing	30.4	−0.24	0.08	0.48	0.30	0.0
4	Crossing	23.7	−0.19	0.33	0.46	0.32	0.0
5	Head on	26.1	−0.36	0.13	0.50	0.35	−10.0
6	Head on	16.6	−0.32	0.38	0.52	0.32	7.0
7	Crossing	27.2	−0.35	0.12	0.51	0.34	0.0
8	Crossing	18.4	−0.32	0.35	0.34	0.31	5.0
9	Head on	21.9	−0.36	0.09	0.50	0.33	0.0
10	Head on	15.2	−0.20	0.35	0.48	0.31	10.0
11	Crossing	35.0	−0.24	0.08	0.48	0.21	0.0
12	Crossing	7.9	−0.37	0.35	0.45	0.30	0.0
13	Head on	24.9	−0.33	0.09	0.53	0.32	−10.0
14	Head on	13.0	−0.18	0.38	0.49	0.32	7.0
15	Crossing	27.6	−0.38	0.10	0.50	0.34	0.0
16	Crossing	14.4	−0.31	0.32	0.28	0.30	5.0

FIGURE 27 Snapshots from the maneuver during run 6. The vehicle is the yellow polyhedron, and the obstacle is the red sphere. The blue line is the vehicle trajectory, while the dashed red line marks the obstacle trajectory. The black arrow denotes the velocity direction of the obstacle, while the blue arrow denotes the velocity direction of the vehicle. The vehicle size is exaggerated for clarity. [Color figure can be viewed at wileyonlinelibrary.com]

avoidance angle to the obstacle, and the resulting maneuver is guaranteed to keep at least a minimum safety distance to the obstacle. To achieve this, the algorithm creates an extended vision cone from the vehicle to the obstacle, and compensates this cone for the obstacle velocity. The flexibility offered by operating in 3D space is then utilized when choosing a safe direction along this cone to avoid the obstacle. The algorithm is only required to know the vision cone

from the vehicle to the obstacle, as well as the obstacle velocity, and not the complete obstacle shape. Thus, algorithm implementation is kept simple, using measurements that are readily available at most platforms.

We have implemented the algorithm on an underactuated underwater vehicle. When such a vehicle turns or pitches, a movement in sway and heave is induced. This movement must be accounted for both during nominal operation and during collision avoidance. To this end, we have proposed a novel Flow frame controller, which steers the direction of the vehicle's velocity direction rather than the vehicle orientation.

Underwater vehicles are often subject to limited surge speed envelopes, both with an upper bound due to limited motor power and a lower bound to retain controllability of the vehicle. The proposed collision
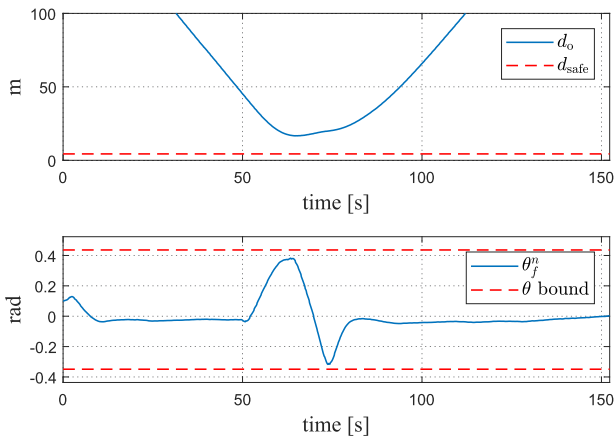

FIGURE 28 The distance d_o between the vehicle and the obstacle during run 6 (top) and Flow frame pitch angle θ_f^n (bottom). [Color figure can be viewed at wileyonlinelibrary.com]
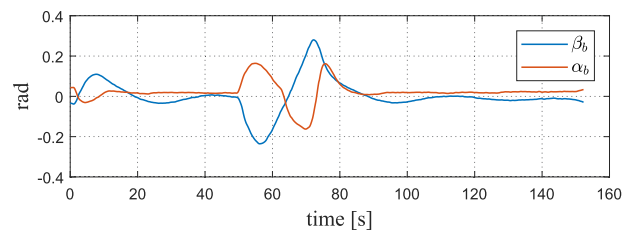

FIGURE 29 The sideslip β_b and angle of attack α_b during run 6. [Color figure can be viewed at wileyonlinelibrary.com]
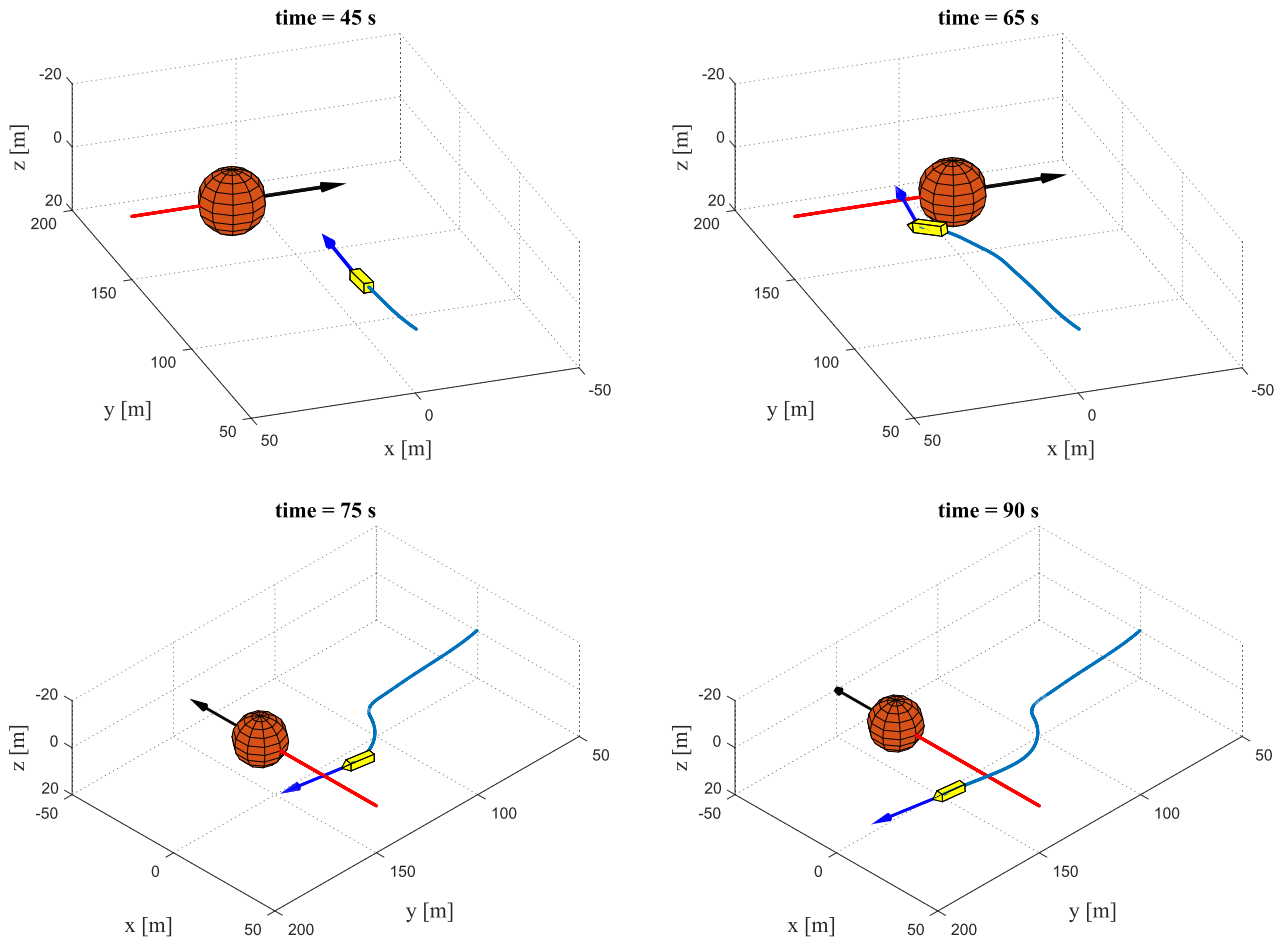
FIGURE 30 Snapshots from run 4, where the obstacle crosses horizontally in front of the vehicle. [Color figure can be viewed at wileyonlinelibrary.com]

avoidance algorithm provides a safe velocity direction using the current vehicle speed as an input. Thus, it can be used to accommodate a variety of desired surge speed trajectories, including ones satisfying limited speed envelopes. We have demonstrated this by implementing the algorithm on

a vehicle where we have put the strict requirement of maintaining a constant desired surge speed throughout the maneuver. Experimentally, we have implemented the algorithm on a vehicle keeping constant forward thrust, showing applicability also to vehicles where the surge speed is not explicitly controlled.

Mathematically, we have provided a detailed analysis of the algorithm and the Flow frame controller applied to a vehicle model containing both kinematics and dynamics in 5 DOF. We have thus been able to derive bounds on the controller parameters and on the minimum safety distance which ensures that the sway and heave speeds are bounded during the maneuver, and that the control signals remain well defined. Informally, the Flow frame controller must
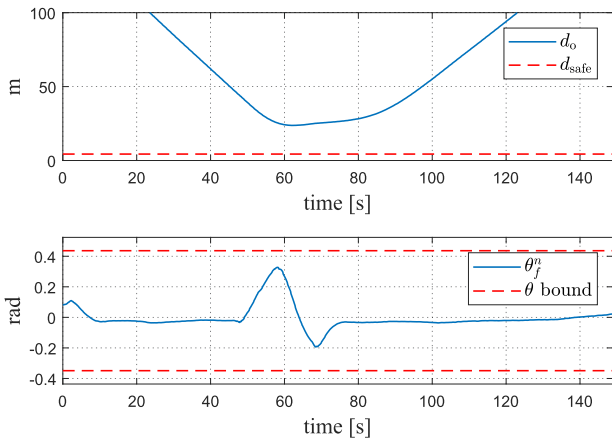

FIGURE 31 The distance d_o between the vehicle and the obstacle during run 4 (top) and Flow frame pitch angle θ_f^n (bottom). [Color figure can be viewed at wileyonlinelibrary.com]
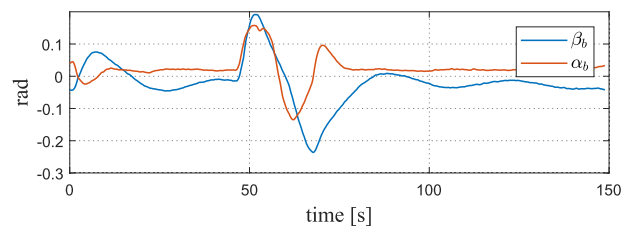

FIGURE 32 The sideslip β_b and angle of attack α_b during run 4. [Color figure can be viewed at wileyonlinelibrary.com]

not be too aggressive, and the safety distance not to small. We have used these results to obtain a minimum obstacle distance at which the vehicle must start the collision avoidance maneuver to be sure that it turns away in time. Finally, we are then able to prove that the entire collision avoidance maneuver is safe and successful.

The theoretical results have been validated through simulations and through experiments on a survey class autonomous underwater vehicle, the Hugin HUS AUV. While the simulations illustrate the performance of the system under ideal conditions, the experiments further strengthen the results by showing the successful performance on a vehicle where the precise model is not known, the underlying controllers are unavailable and there is a presence of sensor noise and disturbances.

As the focus of this paper is on the response of an underactuated vehicle to the collision avoidance algorithm under ideal conditions, a study of sensor uncertainties is beyond the current scope. However, if the obstacle velocity measurements or the vision cone contains uncertainties and noise, the algorithm will require smooth estimates of these parameters. Furthermore, the required avoidance angle and switching distance will increase to guarantee safety even in the presence of noisy and uncertain signals. An extension of the work in this paper to include such a robustness analysis is highly relevant for future work.

This study has mainly been concerned with sparse obstacle scenarios where the vehicle can avoid a single obstacle at a time. While this can be argued to be the most common scenario in an underwater domain, we have also described an extension of the algorithm to multiple, clustered obstacles. A detailed analysis of such a scenario is, however, beyond the scope of this paper and remains a topic of future work. In the case of noncooperating obstacles, it is possible for the vehicle to become trapped if it is surrounded by several close obstacles. Finding limitations on the behavior of the obstacles and on the vehicle maneuvering capabilities to avoid entrapment is an interesting avenue for further research. This study direction is closely related to the case of multiagent systems, where the other agents have implemented the same collision avoidance algorithm. The function used to choose among the safe directions can then be used to implement traffic rules, and the desired surge speed trajectory can be designed to enhance the safety of the system. Thus, it is likely that the complexities associated with a multiagent system can be approached using the flexibility offered by the constant avoidance angle algorithm.

REFERENCES

Børhaug, E., & Pettersen, K. Y. (2006). LOS path following for underactuated underwater vehicle. In *Proceedings of 47th IFAC Conference on Manoeuvring and Control of Marine Craft, Lisbon*, Portugal.

Breivik, M., & Fossen, T. I. (2008). Guidance laws for planar motion control. In *Proceedings of 47th IEEE Conference on Decision and Control*, Cancun, Mexico (pp. 570–577).

Caharija, W., Pettersen, K. Y., Bibuli, M., Calado, P., Zereik, E., Braga, J., & Bruzzone, G. (2016). Integral line-of-sight guidance and control of underactuated marine vehicles: Theory, simulations and experiments. *IEEE Transactions on Control Systems Technology*, 24(5), 1623–1642.

Canny, J., & Reif, J. (1987). New lower bound techniques for robot motion planning problems. In *Proceedings of 28th Annual Symposium on Foundations of Computer Science*, Los Angeles, CA (pp. 49–60).

Chakravarthy, A., & Ghose, D. (1998). Obstacle avoidance in a dynamic environment: A collision cone approach. *IEEE Transactions on Systems, Man, and Cybernetics Part A:Systems and Humans*. 28(5), 562–574.

Chen, Y., Peng, H., & Grizzle, J. (2018). Obstacle avoidance for low-speed autonomous vehicles with barrier function. *IEEE Transactions on Control Systems Technology*, 26(1), 194–206.

Eriksen, B. O. H., Breivik, M., Pettersen, K. Y., & Wiig, M. S. (2016). A modified dynamic window algorithm for horizontal collision avoidance for AUVs. In *Proceedings of* 2016 *IEEE Conference on Control Applications (CCA)*, Buenos Aires, Brazil (pp. 499–506).

Eriksen, B. O. H., Wilthil, E. F., Flåten, A. L., Brekke, E. F., & Breivik, M. (2018). Radar-based maritime collision avoidance using dynamic window. *IEEE Aerospace Conference Proceedings*, Big Sky, MT.

Fiorini, P., & Shiller, Z. (1998). Motion planning in dynamic environments using velocity obstacles. *The International Journal of Robotics Research*, 17(7), 760–772.

Fossen, T. I. (2011). Handbook of marine craft hydrodynamics and motion control, Chichester: John Wiley & Sons.

Fox, D., Burgard, W., & Thrun, S. (1997). The dynamic window approach to collision avoidance. *IEEE Robotics and Automation Magazine*, 4(1), 23–33.

Hagen, I. B., Kufoalor, D. K. M., Brekke, E. F., & Johansen, T. A. (2018). MPC-based collision avoidance Strategy for existing marine vessel guidance systems. In *Proceedings of 2018 IEEE International Conference on Robotics & Automation (ICRA)*, Brisbane, Australia (pp. 7618–7623).

Hagen, P. E., Storkersen, N., Vestgard, K., & Kartvedt, P. (2003). The HUGIN 1000 autonomous underwater vehicle for military applications. In *Proceedings of Oceans* 2003, San Diego, CA (pp. 1141–1145).

Hoy, M., Matveev, A. S., & Savkin, A. V. (2014). Algorithms for collision-free navigation of mobile robots in complex cluttered environments: A survey. *Robotica*, 33(03), 463–497.

Jalving, B., Gade, K., Hagen, O. K., & Vestgard, K. (2004). A toolbox of aiding techniques for the HUGIN AUV integrated inertial navigation system. *Modeling, Identification and Control*, 25(3), 173–190.

Jenie, Y. I., Van Kampen, E.-J., de Visser, C. C., Ellerbroek, J., & Hoekstra, J. M. (2015). Three-dimensional velocity obstacle method for UAV deconflicting maneuvers. In *Proceedings of 2015 AIAA Guidance, Navigation, and Control Conference*, Kissimmee, FL (pp. 1–16).

Jenie, Y. I., van Kampen, E.-J., de Visser, C. C., Ellerbroek, J., & Hoekstra, J. M. (2016). Three-dimensional velocity obstacle method for uncoordinated avoidance maneuvers of unmanned aerial vehicles. *Journal of Guidance, Control, and Dynamics*, 39(10), 2312–2323.

Johansen, T. A., Perez, T., & Cristofaro, A. (2016). Ship collision avoidance and COLREGS compliance using simulation-based control behavior selection with predictive hazard assessment. *IEEE Transactions on Intelligent Transportation Systems*, 17(12), 3407–3422.

Khatib, O. (1986). Real-time obstacle avoidance for manipulators and mobile robots. *The International Journal of Robotics Research*, 5(1), 90–98.

Lalish, E., & Morgansen, K. A. (2012). Distributed reactive collision avoidance. *Autonomous Robots*, 32(3), 207–226.

Panagou, D. (2014). Motion planning and collision avoidance using navigation vector fields. In *Proceedings of 2014 IEEE International Conference on Robotics & Automation (ICRA)*, Hong Kong, China (pp. 2513–2518).

Pettersen, K. Y., & Egeland, O. (1996). Exponential stabilization of an underactuated surface vessel. *Proc. 35th IEEE Conference on Decision and Control*, Kobe, Japan (pp. 1391–1396).

Roussos, G., Dimarogonas, D. V., & Kyriakopoulos, K. J. (2010). 3D navigation and collision avoidance for nonholonomic aircraft-like vehicles. *International Journal of Adaptive Control and Signal Processing*, 24, 900–920.

Savkin, A. V., & Wang, C. (2013). A simple biologically inspired algorithm for collision-free navigation of a unicycle-like robot in dynamic environments with moving obstacles. *Robotica*, 31(6), 993–1001.

Statheros, T., Howells, G., & Maier, K. M. (2008). Autonomous ship collision avoidance navigation concepts, technologies and techniques. *Journal of Navigation*, 61(01), 129–142.

Tam, C., Bucknall, R., & Greig, A. (2009). Review of collision avoidance and path planning methods for ships in close range encounters. *The Journal of Navigation*, 62(2009), 455–476.

van den Berg, J., Snape, J., Guy, S. J., & Manocha, D. (2011). Reciprocal collision avoidance with acceleration-velocity obstacles. In *Proceedings of 2011 IEEE International Conference on Robotics and Automation (ICRA 2011)*, Shanghai, China (pp. 3475–3482).

Wang, C., Savkin, A. V., & Garrett, M. (2018). A strategy for safe 3D navigation of non-holonomic under-actuated robots among moving obstacles. *Robotica*, 36(2), 275–927.

Wiig, M. S., Pettersen, K. Y., & Krogstad, T. R. (2018a). A 3D reactive collision avoidance algorithm for nonholonomic vehicles. In *Proceedings of 2nd IEEE Conference on Control Technology and Applications*, Copenhagen, Denmark (pp. 67–74).

Wiig, M. S., Pettersen, K. Y., & Krogstad, T. R. (2018b). A 3D reactive collision avoidance algorithm for underactuated vehicles. In *Proceedings of 57th IEEE Conference on Decision and Control*, Miami Beach, FL (pp. 1997–2004).

Wiig, M. S., Pettersen, K. Y., & Krogstad, T. R. (2019). Collision avoidance for underactuated marine vehicles using the constant avoidance angle algorithm. *IEEE Transactions on Control Systems Technology* (99, pp. 1–16).

Wilkie, D., Van Den Berg, J., & Manocha, D. (2009). Generalized velocity obstacles. In *Proceedings 2009 IEEE/RSJ International Conference on Intelligent Robots and Systems*, St. Louis, MA (pp. 5573–5578).

APPENDIX: FUNCTIONAL EXPRESSIONS

$$F_{u_b}(u_b, v_b, w_b, r_b, q_b) \triangleq \frac{1}{m_{11}}[(m_{22}v_b + m_{25}r_b)r_b - (m_{33}w_b + m_{34}q_b)q_b - d_{11}u_b], \tag{A1}$$

$$X_v(u_b) \triangleq \frac{m_{25}^2 - m_{11}m_{55}}{m_{22}m_{55} - m_{25}^2}u_b + \frac{d_{55}m_{25} - d_{25}m_{55}}{m_{22}m_{55} - m_{25}^2}, \tag{A2}$$

$$Y_v(u_b) \triangleq \frac{(m_{22} - m_{11})m_{25}}{m_{22}m_{55} - m_{25}^2}u_b - \frac{d_{22}m_{55} - d_{52}m_{25}}{m_{22}m_{55} - m_{25}^2}, \tag{A3}$$

$$X_w(u_b) \triangleq \frac{-m_{34}^2 - m_{11}m_{44}}{m_{33}m_{44} - m_{34}^2}u_b + \frac{d_{44}m_{34} - d_{34}m_{44}}{m_{33}m_{44} - m_{34}^2}, \tag{A4}$$

$$Y_w(u_b) \triangleq \frac{(m_{11} - m_{33})m_{34}}{m_{33}m_{44} - m_{34}^2}u_b - \frac{d_{33}m_{44} - d_{43}m_{34}}{m_{33}m_{44} - m_{34}^2}, \tag{A5}$$

$$Z_w \triangleq \frac{BG_z W m_{34}}{m_{33}m_{44} - m_{34}^2}, \tag{A6}$$

$$F_{q_b}(\theta_b^n, u_b, w_b, q_b) \triangleq -\frac{BG_z W m_{33}}{m_{33}m_{44} - m_{34}^2}\sin(\theta_b^n) + \frac{m_{34}d_{33} - m_{33}(d_{43} - (m_{33} - m_{11})u_b)}{m_{33}m_{44} - m_{34}^2}w_b + \frac{m_{34}(d_{34} - m_{11}u_b) - m_{33}(d_{44} - m_{34}u_b)}{m_{33}m_{44} - m_{34}^2}q_b, \tag{A7}$$

$$F_{r_b}(u_b, v_b, r_b) \triangleq \frac{m_{25}d_{22} - m_{22}(d_{52} + (m_{22} - m_{11})u_b)}{m_{22}m_{55} - m_{25}^2}v_b + \frac{m_{25}(d_{25} + m_{11}u_b) - m_{22}(d_{55} + m_{25}u_b)}{m_{22}m_{55} - m_{25}^2}r_b. \tag{A8}$$